



Nanostructured and nanoporous LiFePO_4 and $\text{LiNi}_{0.5}\text{Mn}_{1.5}\text{O}_{4-\delta}$ as cathode materials for lithium-ion batteries

Sebastian Kraas ^a, Annalena Vijn ^a, Mareike Falk ^b, Boris Ufer ^a, Bjoern Luerßen ^b,
Jürgen Janek ^{b,*}, Michael Fröba ^{a,*}

^a Institute of Inorganic and Applied Chemistry, University of Hamburg, Martin-Luther-King-Platz 6, 20146 Hamburg, Germany

^b Institute for Physical Chemistry, Justus-Liebig-University Giessen, Heinrich-Buff-Ring 58, 35392 Giessen, Germany

A B S T R A C T

Keywords:

Cathode materials
Lithium ion battery
Spinel
Thin films
Lithium iron phosphate
Lithium nickel manganese oxide
LNMO
LFP

Recent developments in the synthesis of nanostructured cathode materials are reviewed for the two prominent compounds LiFePO_4 and $\text{LiNi}_{0.5}\text{Mn}_{1.5}\text{O}_4$, and own results on LiFePO_4 and $\text{LiNi}_{0.5}\text{Mn}_{1.5}\text{O}_4$ with different microstructure are presented. The synthesis of LiFePO_4 composites with porous carbons and the scale up of their synthesis is reported, as well as of nanoporous materials. In the case of $\text{LiNi}_{0.5}\text{Mn}_{1.5}\text{O}_4$ the formation of deteriorating cathode surface films is studied with thin film electrodes and ToF-SIMS depth profiling.

© 2014 Elsevier Ltd. All rights reserved.

Contents

1. Introduction	00
General introduction to the background	00
Purpose of the paper	00
Definition of nanomaterials	00
Advantages/disadvantages of pores	00
Scale-up	00
Methods for nanocasting	00
Thin films	00
2. Review	00
2.1. Nanostructured lithium iron phosphate	00
2.2. Nanostructured lithium nickel manganese oxide	00
2.3. Lithium nickel manganese oxide thin films	00
3. Own results and discussion	00
3.1. Lithium iron phosphate carbon composites	00
3.2. Porous lithium nickel manganese oxide	00
3.3. Lithium nickel manganese oxide thin film model system	00
4. Conclusion	00
Acknowledgments	00
Experimental	00
Lithium iron phosphate (LFP)	00

* Corresponding author. Tel.: +49 (0)641 9934500.

** Corresponding author. Tel.: +49 (0)40 428383100.

E-mail addresses: Juergen.Janek@phys.chemie.uni-giessen.de (J. Janek), Michael.Froeba@chemie.uni-hamburg.de (M. Fröba).

Lithium nickel manganese spinel (LNMO)	00
Materials characterization	00
Electrochemical testing	00
References	00

1. Introduction

The demand for secondary batteries with high capacities, low charging times, long lasting lifetimes and – most important – high safety characteristics is huge. This strong demand led to wide-span research on new battery materials, primarily on anode and cathode materials which together define the theoretical energy density. But finding new materials with new compositions and advanced properties is only one part of the general strategy to improve batteries. As important is the deeper understanding of currently used materials and their optimization toward ultimate performance. For this purpose materials with well-defined composition and microstructure need to be synthesized to study all essential properties in sufficient detail. Especially the energy density, charge and discharge rates, and the surface chemistry in contact with typical battery electrolytes are of great interest.

In the present paper we discuss the properties of two important cathode materials, in particular with respect to nanostructuring: On the one hand we selected lithium iron phosphate (LiFePO₄, LFP) as it is considered as a highly reliable, cheap and safe cathode material with a storage mechanism that is strongly influenced by nanostructuring. On the other hand we selected lithium nickel manganese oxide (LiNi_{0.5}Mn_{1.5}O₄, LNMO) as a promising high voltage material. In both cases we focus on nanostructured materials in order to explore the specific advantages and disadvantages of size reduction.

In the present context we consider a material as being nanostructured once it has structures or morphologies smaller than 1000 nm in up to three dimensions. This includes one-dimensional nanostructures, i.e. wires, two-dimensional nanostructures, i.e. thin films, and three-dimensional nanostructures, i.e. materials with (hierarchical) pore systems. Unconnected nanoparticles belong to the above general definition but are not in the main focus of our discussion. Nonetheless we include them for comparison. In the following we focus primarily on materials with (periodically arranged) nanopores. According to the IUPAC classification nanoporous materials are classified according to their pore size as either microporous (diameter below 2 nm), mesoporous (diameter is between 2 nm and 50 nm) or macroporous (diameter above 50 nm) [1].

The particle morphology plays an important role for the storage properties of insertion and intercalation compounds. The synthesis of particles with small dimensions generally reduces slow bulk transport paths, but increases the surface area and the influence of deteriorating surface reactions with the electrolyte. As battery electrodes need to be porous in order to allow penetration of liquid electrolyte, intrinsically porous materials may offer an advantage with respect to optimal electrode/electrolyte contact. The impact of particle porosity for the energy density of the material is simple to assess, and it is of course always lower for porous material compared to bulk material. A lower energy density is generally good in terms of safety, but bad in terms of final battery size. Faster kinetics of the storage process is perhaps the strongest argument for nanostructuring. Once bulk transport is rate-limiting, then the time constant τ for diffusion is a square function of the diffusion length L (i.e. the particle radius in the case of a spherical particle):

$$\tau = L^2 / D_{\text{Li}} \quad (1)$$

where D_{Li} is the chemical diffusion coefficient of lithium in the storage material (e.g. 10^{-14} – 10^{-13} cm² s⁻¹ for LFP and 10^{-10} – 10^{-7} cm² s⁻¹ for LNMO) [2–4]. In porous materials the diffusion length is reduced, depending on the thickness of the pore walls, and the time for de-/intercalation can be much shorter than for bulk material (cf. very fast mesoporous Li₄Ti₅O₁₂ as an example [5]). During lithium insertion or de-insertion the particle volume of the active phase often changes significantly. For LFP the change in volume from the delithiated to the lithiated phase is e.g. +6.81% [6]. This volume change can be mechanically “buffered” much better by a porous structure, and indeed nanostructuring is a necessity in the case of materials with very large volume effects (e.g. silicon anodes with about 300% volume effect) [7,8]. While the increased surface area of porous materials provides a better access of Li⁺ ions from electrolyte, it also can be subject to severe surface side reactions.

The synthesis of both nanoparticles and nanoporous materials requires more effort than the synthesis of bulk material. The control of the nanoparticle size or the desired pore size can be difficult to achieve, and often expensive templates are required. This leads to the intrinsic problem that usually only small amounts of nanoporous materials are synthesized in laboratory scale batches. Accordingly, the scale up of synthesis is a major issue and potentially costly. But once the synthesis is worked out one ideally ends up with a material with a morphology (particle diameter or pore size for example) that can be well tuned. The adjustable microstructure qualifies nanoporous materials as ideal model systems for studies of the correlation between material morphology and electrochemical performance.

The concept of *nanocasting* describes routes to synthesize mesoporous solids by hard and soft templating [9]. In this paper, we focus on the synthesis of mesoporous cathode compounds by *hard templating*. As templates, well-known periodic mesoporous silica materials such as SBA-15 and KIT-6 or the periodic mesoporous carbon materials such as CMK-3 and CMK-8 were used [10–12]. By a solvent evaporation-induced self-assembly (EISA) process, a new group of periodic mesoporous polymers and carbons has recently been developed, which can also be used as hard templates [13]. The advantage of this new type of structured carbons is a synthesis using a soft template, thus allowing an easier route for scale-up. This synthesis route makes the EISA process a promising route for the industrial use of nanocasting. The procedure of nanocasting is shown schematically in Fig. 1. Firstly, the hard template (e.g. with SBA-15 pore topology) has to be filled with the precursors (e.g. metal salts) (Fig. 1A). The process of pore filling can be carried out in different ways. One standard route is the *wet impregnation* method. Here, the template material is suspended in the precursor solution and either stirred to dryness or filtered off after a certain time. A second way is the *incipient wetness* method, where the volume of the precursor solution corresponds to the pore volume of the template. The second route is beneficial because the formation of bulk material on the outer surface of the template is avoided. Suitable compounds for precursors are usually inorganic salts such as nitrates or hydroxides in aqueous or ethanol solutions. After the filling process the formation of the metal oxide is attained by

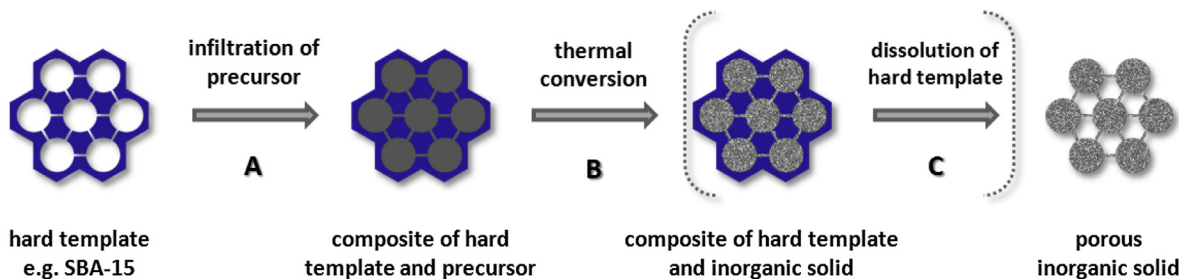


Fig. 1. Schematic illustration of a nanocasting route on SBA-15 morphology.

thermal conversion, and the specific synthetic conditions (e.g. atmosphere, temperature) can be varied according to the desired product and the used template (Fig. 1B). During this step of the synthesis composite materials, for example with carbon, can be prepared. This type of *active phase/carbon composites* with lithium iron phosphate as active phase will be discussed later on. The last step can include the removal of the template if necessary (Fig. 1C). Silica templates can be dissolved in hydrofluoric acid or sodium hydroxide solution. Carbon templates can be decomposed at elevated temperatures, requiring no additional step for template removal. Thus, in some applications, carbon is the best choice as a hard template because of its simpler processing.

To obtain stable porous solids, the interaction of the precursor molecules and the template surface is a key factor. The efficiency of coating of the template by the precursors varies depending on the surface polarity. A silica template provides a polar oxide surface, and its polarity can be controlled by the amount of silanol groups. Most precursors are ionic, hence they interact with surface silanol groups through Coulomb interaction, making it important to use silica materials with high surface concentration of silanol groups. When silica is used as template, the most popular method to fill the pores is the so called *two-solvent* method, a variation of the *incipient wetness* method [14]. Here an aqueous solution of metal compounds (e.g. nitrates) is added to a suspension of silica in *n*-hexane. Because of the different polarities of *n*-hexane and the precursor solution, the aqueous solution is forced into the pores of the silica, supported by the capillary forces of the mesopores. For carbon templates another impregnation technique is required because of its less polar surface. Again, a useful method is a variation of the above described *incipient wetness*, which requires a mixture of precursor solution with dry template material. The polarity of the solvent should be as low as possible to enhance the contact between template and solution. Another technique is the *melt impregnation*, where template and precursors are blended in solid state. By thermal treatment at a certain temperature the molten precursor can infiltrate the pores. Of course only precursors with sufficiently low melting points, lower than their decomposition temperature, can be applied [15–19].

These synthetic routes can be applied to both oxide and non-oxide materials, such as e.g. sulfides or phosphates [14,20]. For example, nanocasting was successfully applied for the first time on a mesoporous carbon called CMK-3 which was casted from SBA-15 silica by Ryoo and coworkers [12]. The first metal oxide yielded in mesoporous form was Cr₂O₃ casted from SBA-15 silica, offering a surface area of 58 m² g⁻¹ (BET) as determined by nitrogen physisorption [21]. Subsequently many groups started to work on the formation of mesoporous inorganic compounds, and today the method of nanocasting is a popular route to obtain them. Many metal oxides such as cerium, iron, and manganese or cobalt oxide have been synthesized with high surface areas up to 198 m² g⁻¹ (BET) via the nanocasting route [22,23].

Ordered mesoporous metal oxides are considered as candidates for a wide range of applications, including energy conversion, storage and catalysis. In heterogenous catalysis, CeO₂, Co₃O₄, Mn_xO_y and their solid solutions with other metal oxides are the most prominent examples. In model-type reactions such as the oxidation of CO or methanol they show performances considerably higher than their bulk counterparts. It should be noted that in these cases ordered pore structures with high surface areas exhibit the best results [24–27]. With regards to energy conversion and storage there are some fields of interest such as solar cells (dye sensitized) and electrode materials. For the former application, mostly TiO₂ in mesoporous forms is used as a container for the light-harvesting dye. Both ordered and disordered mesoporous TiO₂ enhance the solar conversion efficiency by about 50% in comparison to ordinary TiO₂ films [28].

Several mesoporous metal oxides have already been reported as cathode materials for Li ion batteries such as LiCoO₂, β -MnO₂, and Li_{1+x}Mn_{2-x}O₄ spinel [29–31]. Mesoporous LiCoO₂ prepared at low temperature (LT-LiCoO₂) shows a significantly lower capacity fading of 45% after 50 cycles at 0.3 C than bulk LT-LiCoO₂ with a capacity loss of 75%. In case of mesoporous β -MnO₂ the lithiation leads to a phase transition to layered β -Li_xMnO₂. Bulk β -MnO₂ in contrast accommodates virtually no lithium during electrochemical lithiation, and tends to a structural change to LiMn₂O₄ spinel upon lithiation. In contrast, mesoporous β -MnO₂ still offers a capacity of 154 mAh g⁻¹ after 50 cycles with a rate of 2 C and hence can be discussed as a cathode material for lithium ion batteries. Mesoporous lithium manganese spinel Li_{1+x}Mn_{2-x}O₄ was reported by two groups. Jiao *et al.* presented a mesoporous Li_{1.12}Mn_{1.88}O₄ phase with a specific surface area of 90 m² g⁻¹ (BET) which was synthesized by a lithiation step after templating. In a first step, mesoporous Mn₃O₄ was prepared by casting from KIT-6 silica. After removal of the silica matrix and impregnation with lithium hydroxide, the conversion to Li_{1.12}Mn_{1.88}O₄ through heat treatment was carried out. To preserve the mesostructure this heat treatment was performed at low temperature, and thus, the crystallinity of the resulting material was quite low. However, in comparison to the bulk material the capacity retention at rates of 0.3 C and 30 C was higher [29]. Park *et al.* also reported mesoporous LiMn₂O₄ but synthesized it in only one step [31]. Because all metal ions including lithium formed the reaction product in the silica matrix it was possible to carry out the thermal conversion at higher temperatures, hence the crystallinity of the product increased. Unfortunately, lithium ions tend to react with silica forming lithium silicate, so that lithium loss occurs. Nevertheless after dissolution of the silica template Park *et al.* were able to gain a mesoporous spinel with only very little impurities of silicon and a specific surface area of up to 160 m² g⁻¹ (BET). Discharge capacities were about 100 mAh g⁻¹ after 100 cycles at 0.5 C rate with a capacity retention of 85% [31].

Despite the fact that to date lithium ion batteries successfully run in a large number of applications, there are still unsolved problems, concerning e.g. safety issues or capacity fading especially at high temperatures. These problems become even more severe for high voltage materials like $\text{LiNi}_{0.5}\text{Mn}_{1.5}\text{O}_4$ which delivers a voltage of 4.7 V vs. Li/Li^+ , as in this potential range oxidation of common carbonate based electrolytes takes place (see investigations by Lucht and coworkers [32]). Lucht et al. used ethylene carbonate, dimethyl carbonate and diethyl carbonate as electrolyte solvents, which decomposed in a cell using LNMO as cathode materials above 4.85 V, participating in the formation of a layer on the surface of the cathode which is often called “cathode electrolyte interface” (CEI) [33]. To date there is little knowledge about the exact composition, structure and formation mechanism of this film as it is only several tens of nanometers thick. Therefore, all routine analytical tools like XRD or ICP-OES fail since the weak surface signals are superimposed with strong bulk signals of the cathode material. Surface sensitive analytical methods like X-ray photoelectron spectroscopy (XPS) or secondary ion mass spectrometry (SIMS, being very sensitive to lithium together with an outstanding depth resolution of about 2 nm) can provide all necessary information, but lose their surface sensitivity once the studied surfaces are not plane – like in the case of small particles with their strong surface curvature. In particular SIMS requires flat samples, as both the mass and the depth resolution decrease with increasing surface roughness. Therefore, we used a PLD (pulsed laser deposition) based technique to prepare planar thin films of LNMO on suitable substrates. The thin films were deposited by pulsed laser deposition on platinum-coated yttria-stabilized zirconia (YSZ) single crystals since the commonly used metal foils were too rough to achieve sufficiently flat films. Using polished YSZ single crystals a roughness of less than 10 nm was finally achieved. Electrochemical testing of the thin films revealed the same charge–discharge potentials as for technical LNMO electrodes, thus, we developed a suitable model system for a detailed study of surface film formation and its formation mechanism. We like to note that the LNMO films did not contain conducting carbon or binder, and thus, no additional signals complicated the analytical results.

2. Review

2.1. Nanostructured lithium iron phosphate

Reversible lithium storage in LFP material was first reported by Goodenough in 1997 [6].

LFP crystallizes in the olivine structure, and the space group of the orthorhombic crystal structure is $Pnma$ (Fig. 2). The phosphor atoms are coordinated by oxygen in PO_4 tetrahedra, whereas iron and lithium are octahedrally coordinated as FeO_6 and LiO_6 respectively. In the b – c plane each FeO_6 octahedra shares common corners with four other FeO_6 octahedra. Each FeO_6 octahedra shares one edge with a PO_4 tetrahedron and two edges with LiO_6 octahedra. Lithium ions are located in channels running parallel to the b -axis. Therefore LFP is a one dimensional Li^+ conductor. A critical issue of this structure is its low electrical conductivity, combined with slow Li^+ diffusion [2,34]. The one-dimensional channels for Li^+ ion diffusion are easily blocked by irregularities in the material. LFP shows no tendency to ionic disorder beyond lithium mobility at all, but any impurity or stacking fault has a negative influence on the Li^+ conductivity.

The theoretical capacity of LFP is $q_{\text{th}} = 170 \text{ mAh g}^{-1}$ at 3.45 V vs. Li/Li^+ , which is located perfectly within the range of the electrochemical stability of most of the common organic electrolytes used in secondary batteries [6,35]. During the charging process lithium is extracted from LiFePO_4 forming FePO_4 accompanied by an

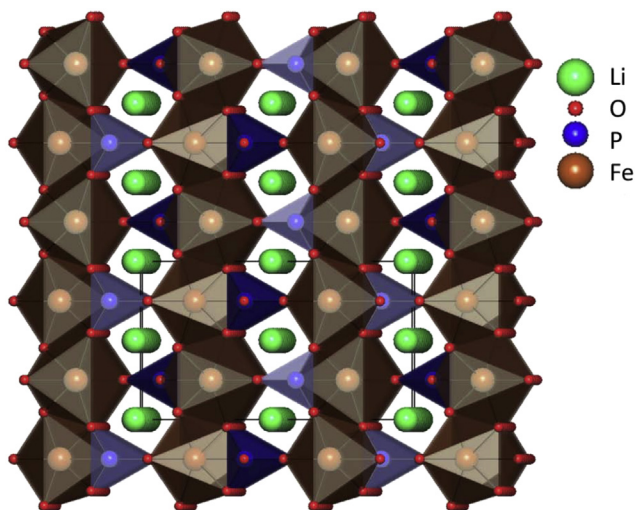


Fig. 2. Crystal structure of lithium iron phosphate (LiFePO_4). Red dots: oxygen, green dots: lithium, blue dots: phosphor, and brown dots: iron. View along the b -axis. (For interpretation of the references to color in this figure legend, the reader is referred to the web version of this article.)

oxidation of $\text{Fe}(\text{II})$ to $\text{Fe}(\text{III})$. Lithium can be completely extracted resulting in a FePO_4 phase which is structurally similar to LiFePO_4 but has a slightly higher density (+2.59%) and a smaller volume (−6.81%) [6]. One reason for the excellent stability of LFP during cycling are the extremely strong covalent P–O bonds. The small volume change, strong P–O bonds and a voltage potential of 3.45 V vs. Li/Li^+ makes LFP an excellent cathode material for use in secondary lithium ion batteries. As mentioned above the existence of either $\text{Fe}(\text{II})$ or $\text{Fe}(\text{III})$ ion containing corner-shared FeO_6 octahedra makes LFP a poor electric conductor. Therefore, improving the electronic partial conductivity of LFP has been a major research target since the first reports of its electrochemical activity.

There are several possibilities to improve the performance of LFP as cathode material. One is decreasing the diffusion length for lithium ions and electrons, by synthesizing small or porous particles. Another one is to synthesize LFP with a coating of an electronically conducting and ion-permeable material. The latter route is mostly achieved by the synthesis of LFP particles with a conductive carbon coating of several nanometers thickness or the synthesis of LFP within the pores of a porous carbon host material.

As explained in the introduction shrinking of the overall particle size leads to shortened diffusions pathways which therefore reduce the time Li ions need to diffuse through the particles. This can result in a better high rate cycling performance of LFP, if also the electronic conductivity throughout the electrode is high. On the other hand small particles can be an issue, since an increased amount of particle-to-particle contacts are needed to support the flow of electrons through the electrode. This contact issue can be circumvented or at least reduced if the LFP particles are embedded into porous carbon. This approach will be discussed later in more detail.

A good example for LiFePO_4 materials performance with reduced diffusion pathways was published by Lim et al. They used the nanocasting route to obtain LFP as porous negative replicas from SBA-15 and KIT-6 silica phases [20] – leading to nanowire LFP structures (SBA-15 template) with a thickness of 7 nm and a specific surface area of $45 \text{ m}^2 \text{ g}^{-1}$ (BET) and hollow LFP structures (KIT-6 template) consisting of hollow spheres with a specific surface area of $105 \text{ m}^2 \text{ g}^{-1}$ (BET) and pores of 5.9 nm (BJH analysis of nitrogen sorption at 77 K). The capacity of the hollow LFP material is found to be higher than nanowire LFP for all examined C rates. However the

nanowire LFP still has a gravimetric capacity of 137 mAh g^{-1} at a rate of 15 C. Both materials also show no capacity fading during the first 80 cycles at 1 C.

As mentioned LFP active material can be improved by adding a carbon layer. This was shown for the first time in 2001 by Armand and coworkers [36]. They synthesized a composite of LFP with carbon and reached the theoretical capacity of LFP (170 mAh g^{-1}) at ambient temperature. This was the first material which benefits from an additional carbon layer, improving vastly the electrochemical performance of LFP in lithium-ion batteries. In comparison Goodenough and coworkers achieved 110 mAh g^{-1} in 1997 [6].

Important for electrochemical performance is a good control of particle size and morphology. This can be achieved by synthesizing LFP particles coated with carbon. Wang et al. used an *in situ* polymerization restriction method to obtain LiFePO_4/C nanocomposites with a core–shell structure [37]. Especially the complete cover of the active material particles with carbon, as shown in Fig. 3, was the subject of their work, as only a fully coated particle supplies efficient pathways for electron transportation. The synthesis is based on a solution of $\text{NH}_4\text{H}_2\text{PO}_4$ and aniline in water from which FePO_4 particles precipitate by adding FeCl_3 solution. The Fe^{3+} at the surface of the precipitated particles starts the oxidative polymerization of aniline to form polyaniline. This polyaniline coating stops the FePO_4 particles from further growth during the following synthesis process in which LiFePO_4/C nanocomposite materials are formed (Fig. 3). With this approach the particle size of the composite can be effectively restricted between 20 nm and 40 nm with a carbon layer thickness of 1–2 nm.

The obtained LiFePO_4/C nanocomposite shows good electrochemical performance. The capacity loss after 1100 cycles is about 5% with a capacity of 168 mAh g^{-1} at a current density of 0.1 A g^{-1} (which is roughly 0.6 C). Also at high current rates (about 60 C) the material still has a capacity of 90 mAh g^{-1} (see Fig. 4).

More recently Yang et al. reported the synthesis of $\text{LiFePO}_4/\text{CNT}$ [38]. The authors used a two-step mechanism consisting of a sol–gel synthesis of LiFePO_4 nanowires followed by *in situ* polymerization of PMMA at the surface of precipitated LiFePO_4 . Restricting the growth of the LFP particles thereby to a diameter of 20–30 nm. During carbonization the PMMA coating of the LFP and excess

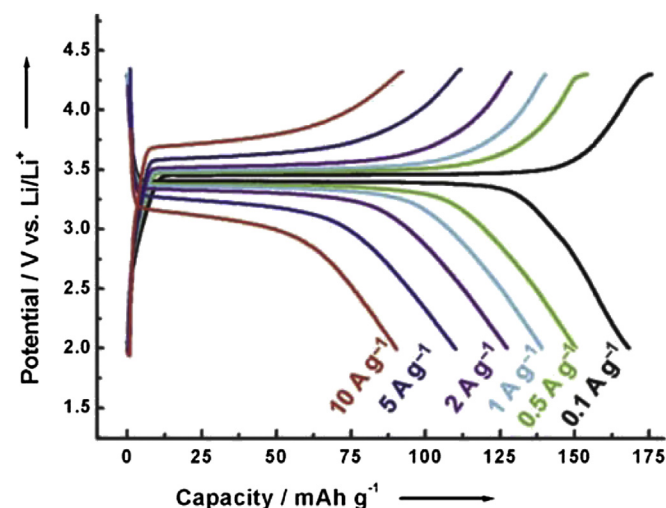


Fig. 4. Charge–discharge capacities for different current rates. Reproduced with permission from WILEY-VCH Verlag GmbH & Co. KGaA, Weinheim [34,37].

PMMA form the CNT coating of the LFP and an additional network of CNT. The authors analyzed three different annealing times (five, ten and 20 h) to find the best time for CNT formation. XANES spectra of the K-edge of carbon indicate that the CNT shell was bound to the LFP core via carboxylate groups. The measured resonance at 288 eV was lower for composites annealed for 20 h than for composites annealed for 5 or 10 h. This difference in LFP and carbon interaction can also be seen in the electrochemical tests. $\text{LiFePO}_4/\text{CNT}$ composites generally show a good performance during cycling. Samples annealed for 10 h have a discharge capacity of 155 mAh g^{-1} (at 0.2 C), with no fading over the first 100 cycles. Even cycling at very high C rates (50 C, 8.5 A g^{-1}) results in a discharge capacity of 65 mAh g^{-1} for samples annealed for 10 h. Whereas samples annealed for 20 h have more than 20% less discharge capacity (120 mAh g^{-1} at 0.2 C). The authors attribute this difference in capacity to the weaker LFP/carbon interaction.

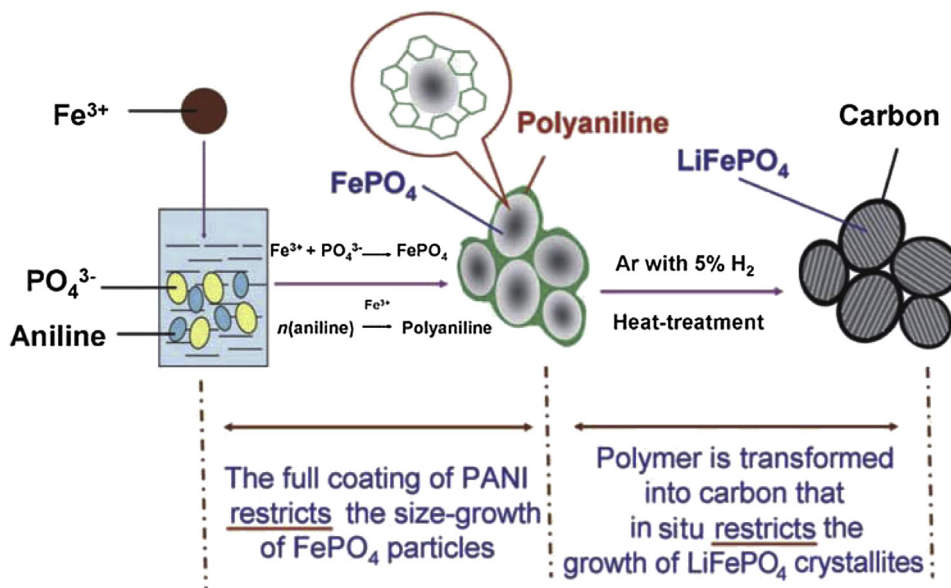


Fig. 3. Synthesis mechanism for the formation of LiFePO_4/C nanocomposites. The polymer shell restricts the growth of the particles during synthesis. Reproduced with permission from WILEY-VCH Verlag GmbH & Co. KGaA, Weinheim [37].

they found in XANES measurements and agglomeration of nanorods in the LiFePO₄@CNT samples annealed for 20 h.

Development of LiFePO₄/C materials with carbon coating has many aspects to be considered, like carbon source, carbon structure (sp^2 or sp^3), carbon thickness and carbon porosity for example [39–41]. For a more detailed overview of carbon coated LFP materials we suggest further reading [42,43].

Another approach to porous LFP is made by Hasegawa et al. [44]. In a two-step synthesis they prepared a macroporous LiFePO₄/C composite. A spinodal decomposition during a sol–gel reaction using PEO as the phase separation inducer and PVP as carbon source is leading to a synthesis without the use of a hard template. PVP is additionally a reducing agent for iron species in the final calcination step. The inorganic-organic hybrid monoliths had a surface carbon content of around 15%. Nitrogen sorption experiments showed a pore volume of around $0.04 \text{ cm}^3 \text{ g}^{-1}$ in the micro- and mesopore range. For calcination temperatures of 600–800 °C specific surface areas of 33–68 $\text{m}^2 \text{ g}^{-1}$ (BET) could be achieved. The samples calcined at 800 °C showed capacities of 137 mAh g^{-1} for 0.1 C and 104 mAh g^{-1} at 1 C. The capacity of these macroporous LiFePO₄/C monoliths are hence lower compared to the previous mentioned mesoporous LiFePO₄ reported by Lim et al. (without carbon coating) [20]. Both the 7 nm nanowires made with SBA-15 hard template and the monolithic LFP material from above have a comparable specific surface area of 44 $\text{m}^2 \text{ g}^{-1}$ and 45 $\text{m}^2 \text{ g}^{-1}$ (BET) respectively. The nanowires from Lim et al. have a thickness of 7 nm whereas the average crystallite size of LFP in the monoliths skeleton of the material synthesized by Hasegawa et al. is 50 nm. This is showing the main influence of the Li diffusion path length mentioned before. The additional carbon surface coating in the monoliths did not help to improve the capacity compared to the very small LiFePO₄ nanowires. Furthermore it seems to be beneficial that the nanowires are part of particles in the micrometer range. This might improve the interparticle contact within the electrode.

Besides the synthesis of inherently porous LFP materials another approach is the combination of a porous carbon host material coated with active material. This new synthesis route allows a specific design of the pore structure of the materials, since there are many possible synthesis routes and applications for porous carbon [45–50].

Doherty et al. used a porous carbon monolith with a hierarchical pore structure of both macro- and mesopores and filled the pores with LFP to obtain a porous LiFePO₄/C composite [51]. The schematic synthesis route is shown in Fig. 5.

Starting with a porous silica monolith the pores are filled with a carbon precursor and subsequently carbonized. In the next step the silica scaffold is dissolved leading to a monolithic carbon material having macro- and mesopores. In a last step the pores are filled with Fe(III) containing LFP precursor solution followed by reduction of the iron to form the new porous LiFePO₄/C composite. The authors examined four different reduction temperatures of 650 °C, 700 °C, 750 °C and 800 °C each resulting in porous composites with 5 nm mesopores and nearly the same surface areas (140–160 $\text{m}^2 \text{ g}^{-1}$, BET) and pore volumes (0.22–0.27 $\text{cm}^3 \text{ g}^{-1}$, BJH) with no correlation of temperature and surface area or pore volume. The diameter of the crystallites which range from 51 nm to 105 nm is consistently increasing with the conversion temperature. Composites annealed at a reduction temperature of 750 °C gave the best discharge capacities of 140 mAh g^{-1} at 0.1 C (Fig. 6). These results are in accordance with the results for the monolithic LiFePO₄/C composite made by Hasegawa et al. Both materials have nearly the same crystallite sizes and hence a similar capacity at 0.1 C.

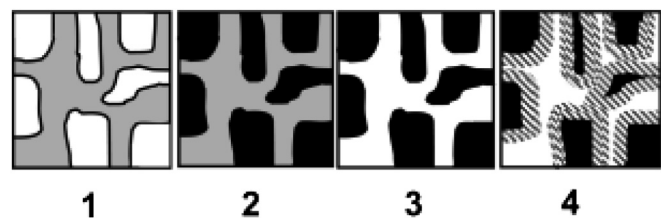


Fig. 5. Scheme for synthesis of a porous carbon monolith and the corresponding composite of carbon and LiFePO₄. Step one is the preparation of a meso/macroporous silica monolith. These pores are filled with carbon precursor, which is carbonized (step 2). Following the chemical removal of silica (step 3) is infiltration of LFP precursor into the pores and calcination (step 4).

Reproduced with permission from the American Chemical Society [51].

Jägermann and coworkers used 3D porous carbon foams as support to study the optimal route to get LiFePO₄/C composites [52,53]. Into commercial available carbon foam with micro-, meso- and macropores LiFePO₄ was filled by a Pechini-assisted reversed polyol process. The best synthesis conditions were 600 °C at an annealing time of 5 h, which results in composites with a discharge capacity of 105 mAh g^{-1} . Thus, a simple way to get LFP/C composites can be the use of commercial carbon, although the achieved capacity is not very high compared to other optimized carbon hosts.

2.2. Nanostructured lithium nickel manganese oxide

Lithium-containing spinels and layered compounds (oxides) are well known active materials for lithium-ion batteries. The layered compound LiCoO₂ was first introduced as a cathode material in 1980 by Goodenough and coworkers and is still one of the most important cathode materials for Li-ion batteries [54]. It offers a potential of 3.9 V vs. Li/Li⁺ and a specific capacity of 150 mAh g^{-1} . Another material which attracts the attention of many research groups is lithium manganese oxide spinel (LiMn₂O₄) and its doped derivatives. It shows a potential of 4.0 V vs. Li/Li⁺ and a theoretical capacity of 120 mAh g^{-1} . In contrast to layered LiCoO₂, LiMn₂O₄ exhibits better safety behavior upon overcharging. In addition, it is environmentally benign and of lower cost. To circumvent some disadvantages which are related to LiMn₂O₄ like decomposition at elevated temperatures, irreversible capacity loss by deep discharge and the relatively low specific capacity, doping of the material is the major strategy, and nickel became the most important doping element. The resulting Ni doped spinel LiNi_{0.5}Mn_{1.5}O₄ offers a high potential of 4.7 V vs. Li/Li⁺ and a theoretical capacity of 147 mAh g^{-1} [55]. It consists of a cubic closed packed array of

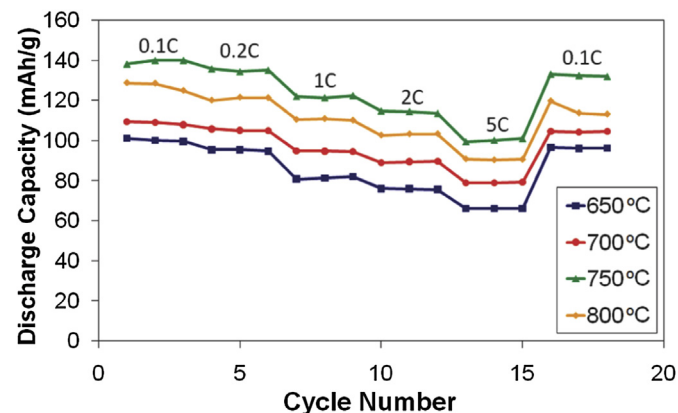


Fig. 6. Charge–discharge capacities for different C rates of a LiFePO₄/C composite. Reproduced with permission from the American Chemical Society [51].

oxygen ions, where lithium ions occupy one eighth of the tetrahedral sites and the transition metal ions reside in half of the octahedral sites (Fig. 7).

$\text{LiNi}_{0.5}\text{Mn}_{1.5}\text{O}_4$ occurs in two different crystal structures which are determined by the distribution of the transition metal ions in the octahedral sites. And this distribution is controlled by the oxygen content, i.e. by a deficiency of oxygen. To clarify this, the molecular formula is often written as $\text{LiNi}_{0.5}\text{Mn}_{1.5}\text{O}_{4-\delta}$, where δ indicates the deficiency in oxygen. With a stoichiometric amount of oxygen ($\delta = 0$, $\text{LiNi}_{0.5}\text{Mn}_{1.5}\text{O}_4$, $P4_332$) the nickel ions are present in the oxidation state of +2 and manganese ions in the oxidation state +4. Because of the different radii of nickel and manganese ions (Ni^{2+} : 69 pm, Mn^{4+} : 53 pm, high spin) and, therefore, the different bond length between oxygen and metal ion, the occupied octahedral sites are distorted. If the spinel shows an oxygen deficiency ($\delta > 0$), the missing negative charge has to be balanced by the reduction of manganese from +IV to +III. The change in size of the manganese ion (Mn^{3+} : 65 pm, high spin) leads to a minimization of strain in the structure. The material then crystallizes in the $Fd\bar{3}m$ space group, also called “disordered LNMO” when the ions are distributed randomly in the octahedral sites, while the $P4_332$ -type structure is formed when the metals in octahedral sites are ordered (ordered LNMO) [56]. The difference between the two structures is also reflected in their electrochemical performance [57]. Fig. 8a shows the charge and discharge curves of $\text{LiNi}_{0.5}\text{Mn}_{1.5}\text{O}_{4-\delta}$ in $P4_332$ and $Fd\bar{3}m$ structure. As expected the curves of the $P4_332$ structure show only one plateau for the redox reaction of Ni^{2+} to Ni^{4+} at about 4.7 V. The curves of the $Fd\bar{3}m$ structure show an additional plateau at about 4.0 V attributed to the presence of Mn^{3+} and the related redox reaction to Mn^{4+} . The same information can be obtained from a graph of the differential capacity curves (Fig. 8b). They show the typical peaks at about 4 V (inset) and 4.7 V. A significant difference between the two phases is seen in the redox peaks of nickel. Both oxidation and reduction peaks located at lower potential of the disordered phase ($Fd\bar{3}m$) are shifted to lower values compared to the ordered phase ($P4_332$). This can be ascribed to the different structural changes the two space groups undergo during the de-/intercalation of lithium and illustrate the facilitation of lithium removal from the structure. The reasons are illustrated in detail by X-ray diffraction patterns. Kim et al. describe a topotactic two-phase transition for

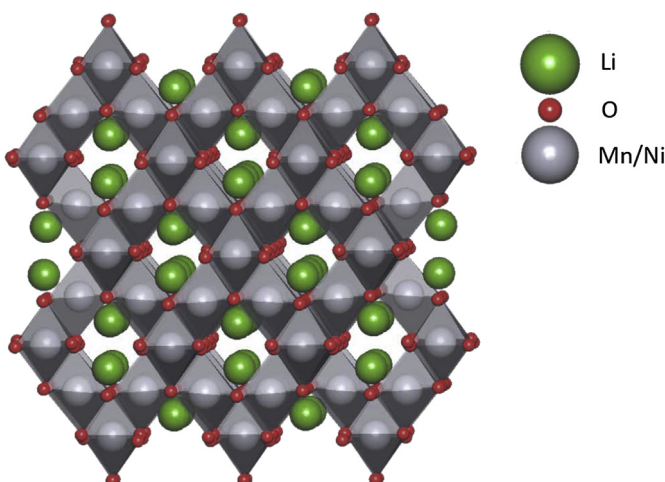


Fig. 7. Structure of $\text{LiNi}_{0.5}\text{Mn}_{1.5}\text{O}_4$ spinel showing parallel arranged chains of transition metals, which are stacked rotated by 90°. Red dots: oxygen, green dots: lithium, gray dots: manganese and nickel in ratio 3/1. View along the b -axis. (For interpretation of the references to color in this figure legend, the reader is referred to the web version of this article.)

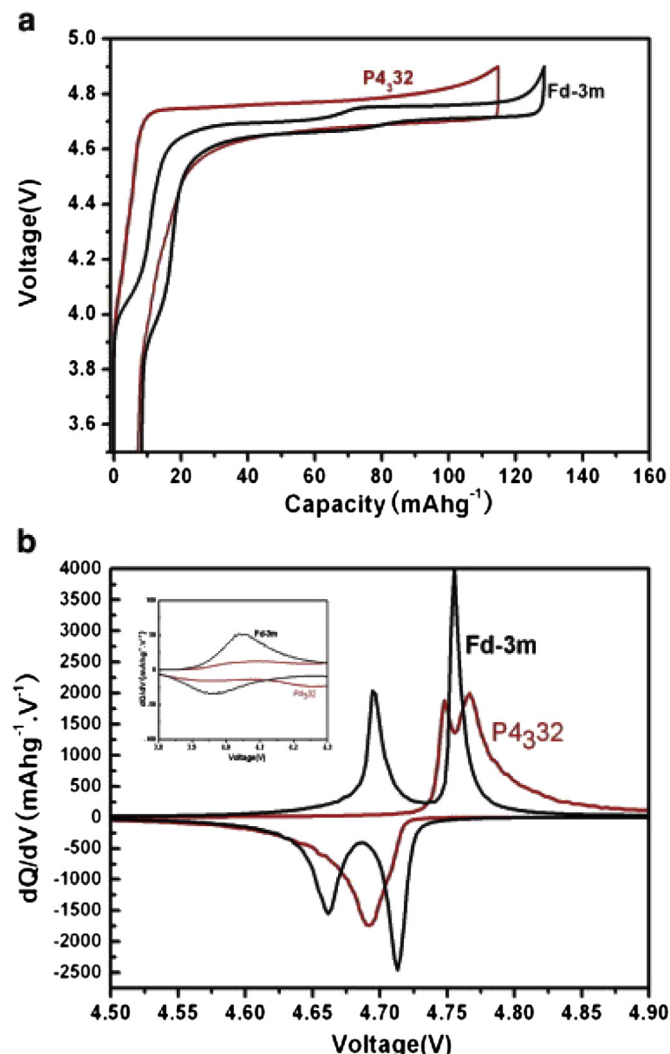


Fig. 8. (a) Typical charge and discharge curves of two polymorphs and (b) corresponding differential curves.
Reproduced with permission of Elsevier [58].

$\text{Li}_{x}\text{Ni}_{0.5}\text{Mn}_{1.5}\text{O}_{4-\delta}$ with the space group $Fd\bar{3}m$ during cycling and a phase transition including three phases for the space group $P4_332$ in a nanocrystalline solid. As shown in the *ex situ* X-ray diffraction patterns (Fig. 9), for disordered materials with $Fd\bar{3}m$ space group, a shift of peaks to higher 2θ values is observed in a region up to $x = 0.5$ (whereas x denotes the stoichiometry of Li and is necessarily correlated to the state of charge), corresponding to a reduction of the cell parameter ($x = 0, a = 8.17 \text{ \AA}$). From $x = 0.5$ up to $x = 0.04$, a second cubic phase with a cell parameter of 8.00 \AA appears. At fully charged state ($x = 0.04$), the second cubic phase exists exclusively (Fig. 9). For the ordered spinel ($P4_332$), two phase transitions are seen during the charging process (Fig. 10). When the extent of charging reaches $x = 0.75$, a second phase appears ($a = 8.08 \text{ \AA}$) and dominates at $x = 0.5$. With further progress of lithium removal a third phase ($a = 7.99 \text{ \AA}$) is formed, replacing the second phase at the stage of complete charge [57]. From these information it is obvious that the redox peaks of nickel are shifted to lower values because of the different phases appearing while dis-/charge for the two space groups $Fd\bar{3}m$ and $P4_332$. The phases for fully charged state ($x = 0.04$) are nearly the same related to the cell parameter (8.00 \AA for $Fd\bar{3}m$ and 7.99 \AA for $P4_332$). However, $\text{Li}_{x}\text{Ni}_{0.5}\text{Mn}_{1.5}\text{O}_{4-\delta}$ ($Fd\bar{3}m$) undergoes only a single phase transition, which affects the crystal

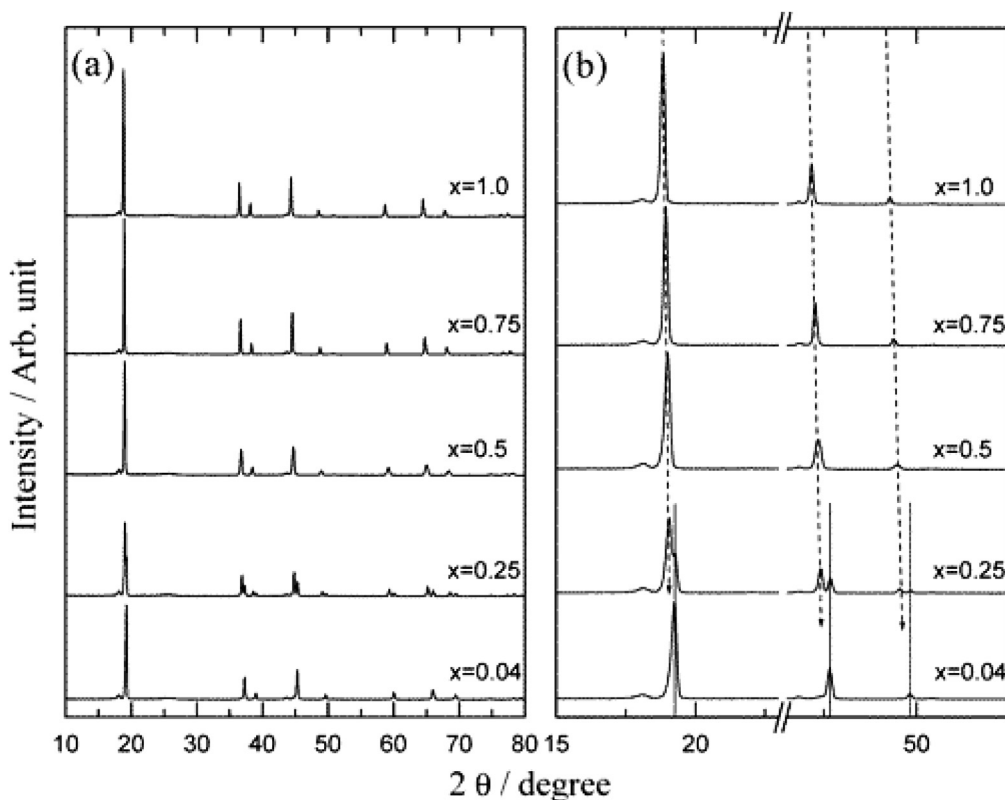


Fig. 9. Ex-situ X-ray diffraction (XRD) patterns of $\text{Li}_x\text{Ni}_{0.5}\text{Mn}_{1.5}\text{O}_{4-\delta}$ ($\text{Fd}\bar{3}m$) electrodes at different states of charge. Reproduced with permission of the American Chemical Society [57].

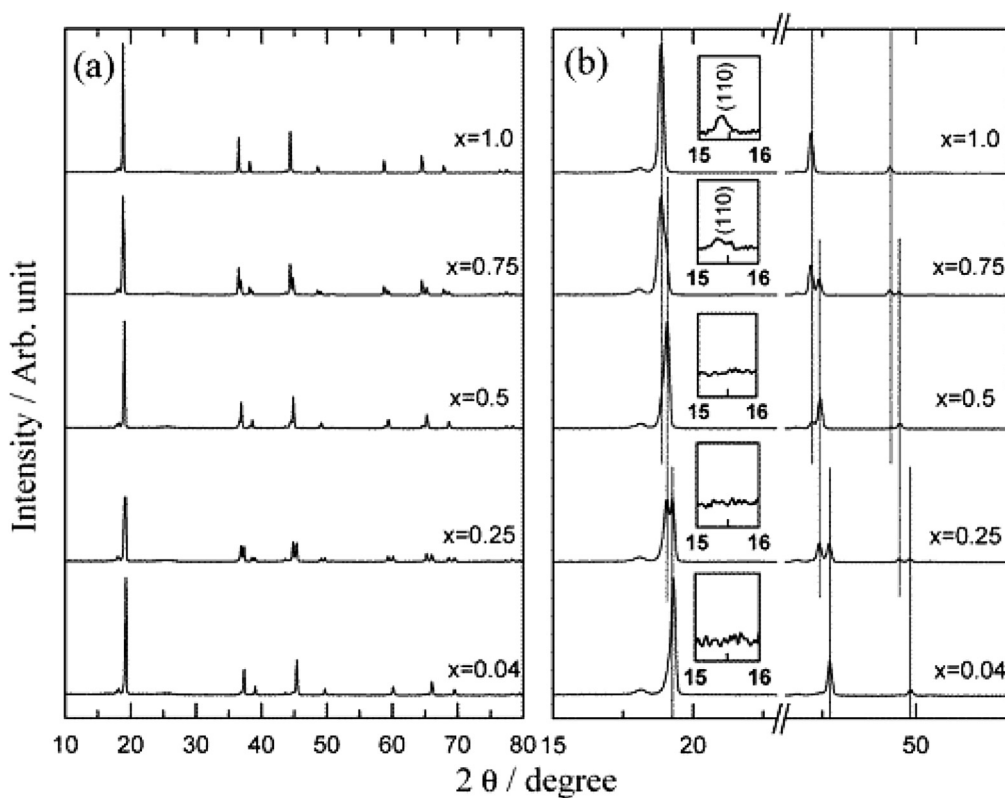


Fig. 10. Ex-situ X-ray diffraction (XRD) patterns of $\text{Li}_x\text{Ni}_{0.5}\text{Mn}_{1.5}\text{O}_4$ ($\text{P}4_3\text{2}2$) electrodes at different states of charge. Reproduced with permission of the American Chemical Society [57].

structure far less than the two phase transitions of the $P4_332$ structure. This leads to an easier extraction of lithium from the material, hence it takes place at lower voltages. At full charge the two phases behave more similar, hence the extraction of lithium is limited by the same conditions and the second peak is shifted far less.

On the contrary, the results presented by Wang et al. show that three phases show up during lithium de-/intercalation for both space groups $Fd\bar{3}m$ and $P4_332$ [58]. In case of the $Fd\bar{3}m$ phase the Bragg peaks are shifted during Li^+ deintercalation between $1.0 \geq x \geq 0.6$ to lower angles in the same cubic symmetry. At lower lithium content a second phase with a cell parameter of $a = 8.08 \text{ \AA}$ is formed. Upon further removal of the lithium a third phase appears ($a = 8.00 \text{ \AA}$) (Fig. 11a) while the first phase disappears. For the ordered spinel ($P4_332$) also a second phase can be observed at $x = 0.7$ ($a = 8.08 \text{ \AA}$). Prior to the phase transition, the shifts of cell parameter are smaller for ordered materials (0.01 \AA) than those for the disordered spinel (0.05 \AA). At $x = 0.5$ a third phase appears ($a = 8.01 \text{ \AA}$, Fig. 11b) while the first phase is still visible, hence there exists a three phase mixture at fully charged state of the cell. These observations were made for materials with particles of submicron size. Although a two phase transition was found for both ordered and disordered spinel, it can be assumed that the existence of a three phase mixture at the end of charge for the ordered spinel limits its electrochemical performance since parts of the electrode material are electrochemically inactive. The difference between the results of the groups of Wang and Kim can be explained by different crystallite sizes utilized for the investigations. In nanocrystalline solids the miscibility gap is narrowed. Therefore the amount of the solid solution increases during decrease of the lithium content. This is illustrated by a calculation of the free mixing energy, which depends among others on the particle volume. Hence, the gain of energy for phase separation is decreased for small particles and a solid solution is preferred [59]. Because of this, the cell parameters of the solid solution and the final phase are more similar so that there is no interphase needed to compensate these differences [58]. Nonetheless, both reports suggest that the disordered spinel ($Fd\bar{3}m$) is a better choice as cathode material.

As discussed in the previous section, the crystal structure of $LiNi_{0.5}Mn_{1.5}O_{4-\delta}$ is critical for the battery performance. The quaternary solid solution of the oxides of lithium, nickel and manganese is very difficult to handle because of the various phases that can be formed – in particular once oxygen deficiency is allowed. Therefore, an accurate control of the synthesis conditions is highly important to obtain the desired crystal structure in good quality.

The ternary phase diagram of lithium, manganese and nickel oxide as developed by McCalla et al. shows that various phases and phase mixtures (solid solutions) can exist in lithium nickel manganese oxide solid solutions [59,60]. Three single phase regions, a spinel, a cubic and a layered rock-salt phase are shown, which are indicated by red lines in Fig. 12 [59], but most of the compositions within the quaternary system of lithium, nickel, manganese and oxygen exist as heterogeneous mixtures of two solid solution phases. As one can see by the comparison of the two ternary phase diagrams in Fig. 12, both obtained by synthesis in oxygen atmosphere at a temperature of $800 \text{ }^\circ\text{C}$ but with different cooling rates, the variation of the synthesis conditions affects the system significantly. The region for the formation of the spinel phase is relatively small for a slow cooling rate and enlarges by quenching the sample. The upper boundary of the spinel phase moves upward by quenching the reaction, caused by reduced oxygen content, which prevents the occurrence of additional phases.

Thus almost every synthetic route to gain $LiNi_{0.5}Mn_{1.5}O_{4-\delta}$ results in the formation of byproducts, which makes it even more

challenging to obtain phase-pure $LiNi_{0.5}Mn_{1.5}O_{4-\delta}$. This complicates the use of the spinel as a cathode material since the active mass is decreased and side reactions are promoted, leading to the degradation of the active material.

To increase the stability of the spinel various techniques have been applied. One method is further doping with additional metal ions such as Cr, Fe or Ti. These can enhance the disordering of metal ions in the octahedral sites, which leads to the formation and stabilization of the $Fd\bar{3}m$ phase. Furthermore foreign ions suppress the formation of rock salt type byproducts [61–66].

Another approach to stabilize cathode material especially against reaction with the electrolyte is to coat the material with an inert surface layer such as ZnO or SnO_2 . Thus, oxidation of common carbonate electrolytes operated at potentials above 4.5 V can be avoided. These coatings avoid the dissolution of Mn(III) into the electrolyte promoted by HF, hence the cycling performance is improved and there is nearly no capacity fading perceivable over 50 cycles even at elevated temperatures ($55 \text{ }^\circ\text{C}$, 0.3 C) [67].

2.3. Lithium nickel manganese oxide thin films

Up to now only a small number of studies on LNMO thin films have been reported. Arrebola et al. use the spin coating process to

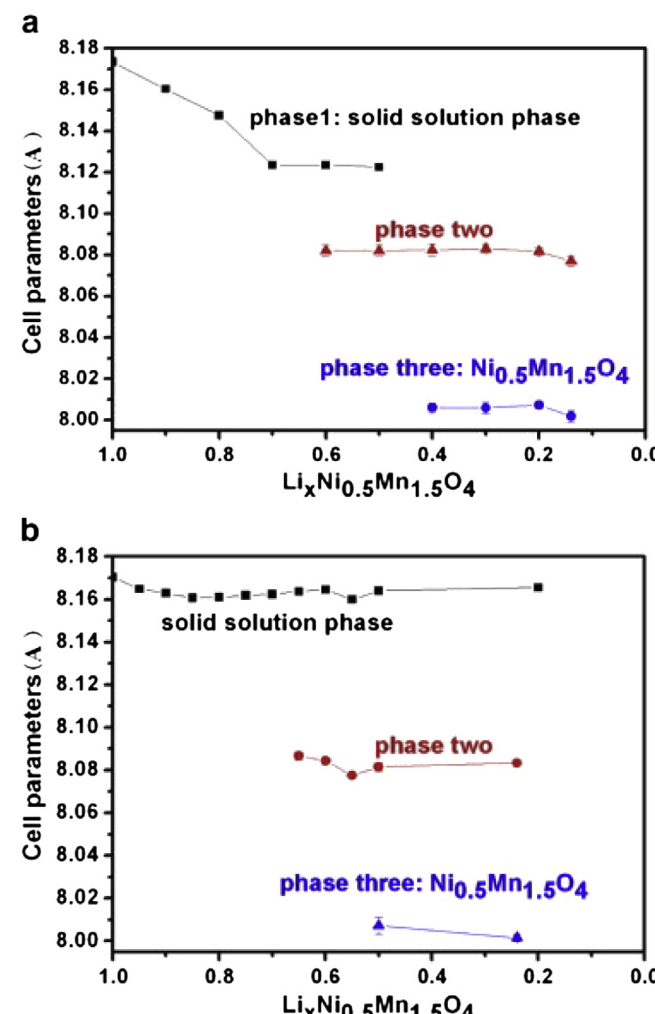


Fig. 11. Evolution of lattice constants of different phases during different Li^+ deintercalation depths (a) $Fd\bar{3}m$ structure and (b) $P4_332$ structure. Reproduced with permission of Elsevier [58].

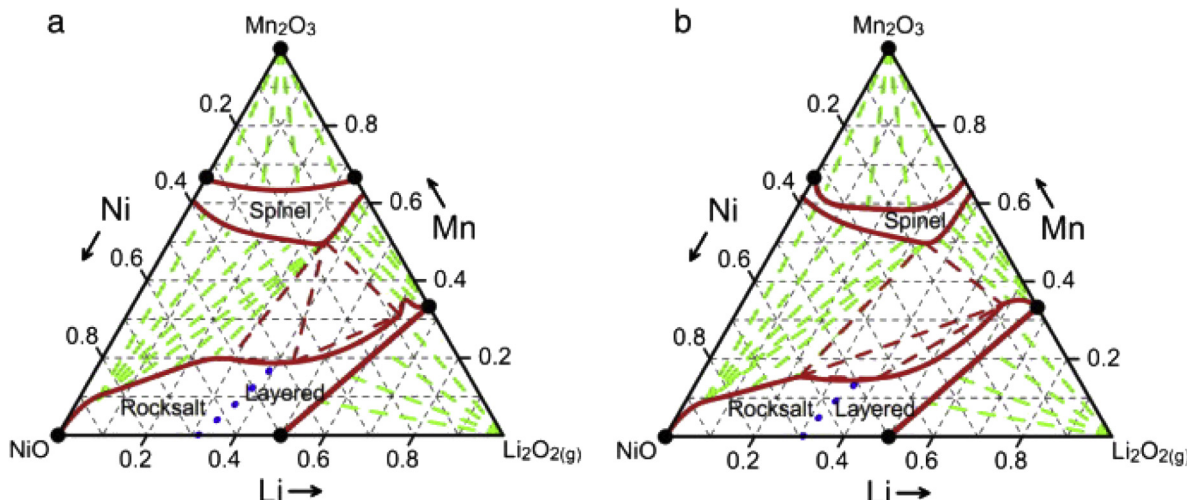


Fig. 12. Ternary phase diagrams for the study of the phase field of $\text{LiNi}_{0.5}\text{Mn}_{1.5}\text{O}_{4-\delta}$. (a) Samples were heated in oxygen and then quenched from $800\text{ }^{\circ}\text{C}$. (b) Phase diagram obtained when the heating was done in a flow of oxygen at $800\text{ }^{\circ}\text{C}$ and the normal cooling rate was used. Red solid lines are boundaries to single-phase regions, the blue dotted lines represent a phase transition, green dashed lines between cubic and layered rock salt structures are tie-lines and the red dashed lines are tie-lines bounding of three-phase regions. (For interpretation of the references to color in this figure legend, the reader is referred to the web version of this article.) Reproduced with permission of Elsevier [59].

deposit LNMO on gold substrates [68]. Their investigations reveal a higher coulombic efficiency for thicker samples, presumably due to hindrance of the contact between electrolyte and the gold substrate, which catalyzes the electrolyte decomposition. On the other hand thicker samples show lower capacity values as the increasing thickness results in a decreased inter-particle connectivity together with a degraded electronic conductivity due to the absence of conductive carbon in an increasing layer of a relative poor electronically conducting material.

Xia et al. optimized LNMO thin films on both silicon wafers and stainless steel by pulsed laser deposition (PLD) and studied the intrinsic properties of the electrode material such as lithium diffusivity without presence of binder and conductive carbon [69,70]. Besides the temperature (below $600\text{ }^{\circ}\text{C}$ no sufficiently flat thin films can be deposited) the oxygen partial pressure during

deposition is an important parameter since both crystallinity and purity are improved with increasing partial pressure [70]. The lithium diffusion coefficient of the thin films was determined in the range of 10^{-12} – $10^{-10}\text{ cm}^2\text{ s}^{-1}$ and reveals a maximum at half lithium filling, where a minimum in the self-diffusion coefficient occurs caused by reduced vacancy mobility due to Li/vacancy ordering in the electrode. Kinetic and transport parameters of LNMO thin films were also studied by Mohamedi et al. using impedance spectroscopy [71]. Their experiments show two minima in the apparent chemical diffusion coefficient at potentials close to the peak potentials in cyclovoltammograms (CV), but the authors present no explanation for this phenomenon.

Nevertheless application of thin films is beneficial in these investigations as the influence of conductive carbon and binder is excluded. Beside the lack of binder and carbon together with the

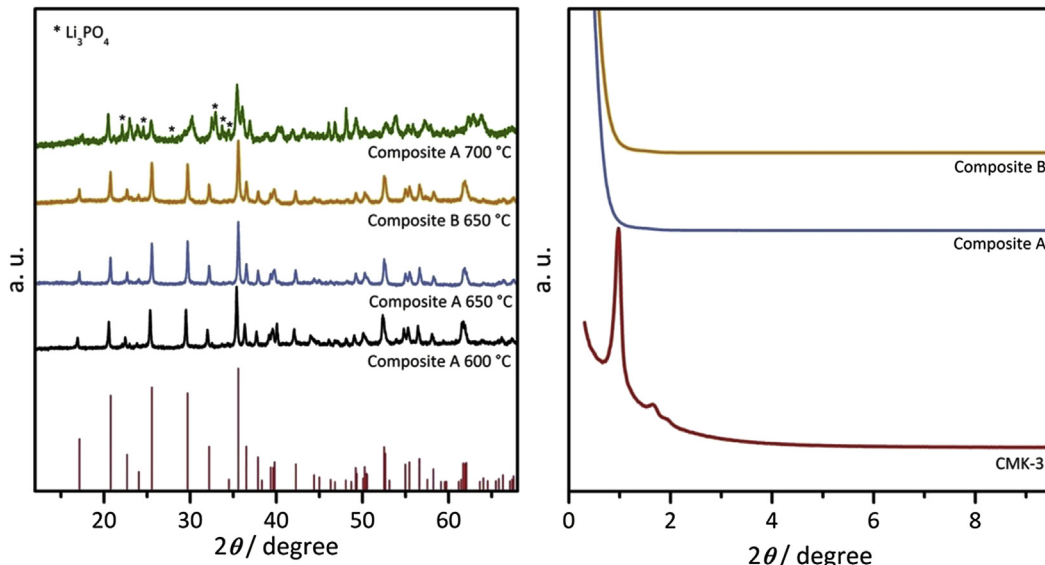


Fig. 13. Powder X-ray diffraction patterns of lithium iron phosphate in CMK-3 composites A and B are displayed on the left side. Red bars show the pattern of LFP (PDF-01-083-2092) for comparison. On the right side the small angle X-ray patterns of the composites A and B annealed at $650\text{ }^{\circ}\text{C}$ and the used CMK-3 scaffold are shown. (For interpretation of the references to color in this figure legend, the reader is referred to the web version of this article.)

well-defined geometry and surface area another benefit of the thin film model systems is the ability to prepare uniform coatings with controlled thickness. This was used by Baggetto et al. to study the beneficial effect of surface coating on the LNMO cathode material concerning cycling stability [33]. Films were deposited on platinum-covered Al_2O_3 substrates by magnetron sputtering and either ZnO or lithium phosphorus oxynitride (LiPON) coatings were ablated by reactive sputtering. Baggetto's experiments show a reduction of the irreversible capacity due to the coating and indicates that electron transfer is prevented on the cathode surface. At the interface between coating and electrolyte coulombic losses are reduced due to electrolyte decomposition and SEI-like layer formation. Moreover, the performance with lithium conducting LiPON is better than with ZnO.

3. Own results and discussion

3.1. Lithium iron phosphate carbon composites

Our experimental approach was to prepare composites of porous carbon with LiFePO_4 . The approach is focused on the synthesis of well-defined porous carbon structures to investigate their influence on active materials like LiFePO_4 . We used the nanocasting process to synthesize mesoporous carbon hosts from SBA-15 and KIT-6 silica hard templates. This route offers a wide choice of carbon precursors, which can be used in the synthesis. The most prominent examples of porous carbons made from SBA-15 or KIT-6 silica and sucrose are CMK-3 and CMK-8 respectively [11,12]. We used the sucrose based porous carbon CMK-3 structures as a reference for composites made of LiFePO_4 and functional carbon materials.

The pores of the CMK-3 carbon were filled via the *incipient wetness* method. This method was chosen because it allows a very good control of the pore filling. With up to 10 consecutive impregnation steps a pore filling of about 70 vol% (composite A) and 60 vol% (composite B) was reached. The infiltration of the LiFePO_4 precursor solution into the pores was followed by the conversion into LiFePO_4 . This took place in a forming gas atmosphere to reduce $\text{Fe}(\text{III})$ ions to $\text{Fe}(\text{II})$. In Fig. 13 the XRD patterns for samples of composite A which are heat treated for 6 h at three

different temperatures are shown. At lower temperatures (600–650 °C) only LiFePO_4 is found (see Fig. 13) whereas at higher temperature an additional lithium phosphate phase is detected. To avoid this impurity and to obtain a highly crystalline material a synthesis temperature of 650 °C was used [44]. As it can be seen on the right side of Fig. 13 the used CMK-3 exhibits the typical X-ray diffraction pattern corresponding to a hexagonal arrangement of the cylindrical mesopores. Neither the composite A nor the composite B show any reflexes. This is due to the destructive interference between the X-ray scatters of the pore walls and guest species, indicating a high filling of the pores with LFP.

The used carbon has to provide a high surface area and also a high pore volume, such that after filling of the pores there is still enough porosity left for the electrolyte to get in contact with LFP. The nitrogen sorption isotherms of the silica template, the carbon and both of the composites are presented in Fig. 14. The nitrogen sorption isotherms and the calculated pore size distributions of the used carbon and its silica template SBA-15 both show a type IV isotherm and H1 hysteresis typical for mesoporous materials. For the CMK-3 carbon the hysteresis between 0.85 and 0.95 p/p_0 is resulting from inter-particle porosity. The pore size of the carbon (5.37 nm, QSDFT desorption branch) is lower than that for the silica (9.77 nm, QSDFT desorption branch). This is due to the fact that the pores of the carbons are the former pore walls of the silica. The specific surface areas (BET) and pore volumes as well as the pore diameters are given in Table 1. The sucrose based CMK-3 has a surface area of $1253 \text{ m}^2 \text{ g}^{-1}$ and a pore volume of $1.33 \text{ cm}^3 \text{ g}^{-1}$. Analysis of the physisorption isotherms of the composite (Fig. 14) reveals that the specific surface area (BET) and also the pore volumes are significantly smaller than for pure CMK-3 carbon (see Table 1). As CMK-3 itself is not affected by temperatures of 650 °C in forming gas atmosphere, a destruction of the pore system is no reason for the decreasing pore volume. The smaller pore volume ($0.12 \text{ cm}^3 \text{ g}^{-1}$ for composite A and $0.29 \text{ cm}^3 \text{ g}^{-1}$ for composite B) shows that the LFP is formed inside the carbon mesopores.

For electrochemical measurements electrodes of both composites sample were prepared and tested in Swagelok T-cells against lithium. Electrolyte was 1 M LiPF_6 in EC/DMC 1:1 w/w. In Fig. 15 CV diagrams of both samples (A, B) are displayed. Both composites

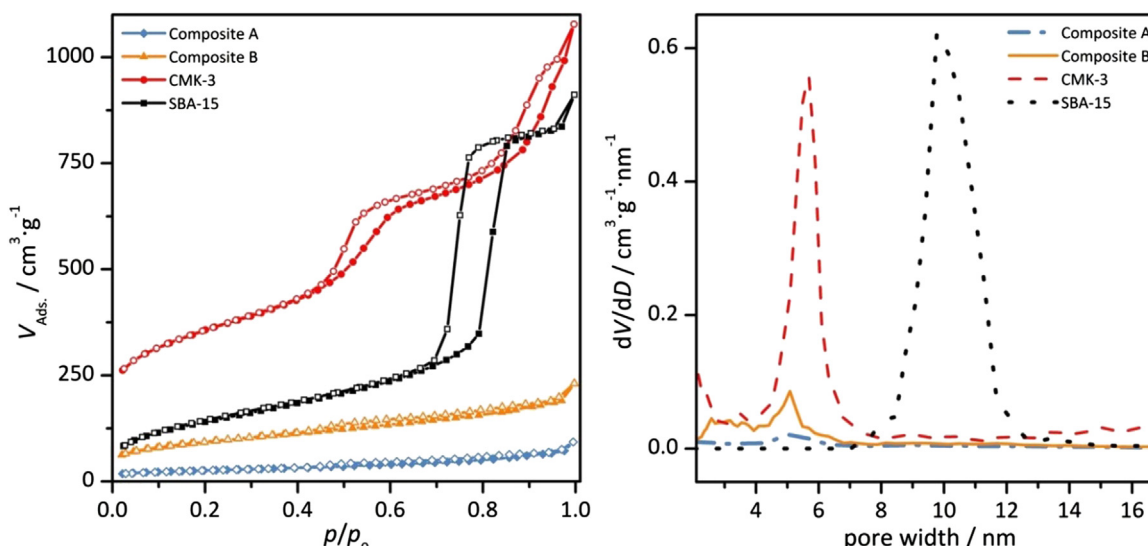


Fig. 14. Nitrogen physisorption isotherms (77 K; filled symbols: adsorption; empty symbols: desorption) for the silica template SBA-15 (black), the porous carbon CMK-3 (red) and both of the LFP/CMK-3 composites (composite A in blue and composite B in orange) are shown on the left side. The right side exhibits the respective pore size distributions, determined by QSDFT analysis of desorption branches (cylindrical pores). (For interpretation of the references to color in this figure legend, the reader is referred to the web version of this article.)

Table 1

Summary of nitrogen physisorption data analysis for the CMK-3 carbon and its template SBA-15 and the corresponding composites A and B.

Sample	$S_{\text{BET}}/\text{m}^2 \text{ g}^{-1}$	Pore size/nm	Pore volume/cm $^3 \text{ g}^{-1}$
SBA-15	457	9.77	1.27
CMK-3	1253	5.37	1.33
Composite A	91	5.01	0.12
Composite B	330	4.84	0.29

show the typical oxidation and reduction peaks of LiFePO₄ without any other reactions within the range of 2–4.5 V. Discharge capacities based on the mass of LiFePO₄ are presented in Fig. 15. Sample B with a lower degree of pore volume filled has the better capacity. These results show that the degree of pore filling and accessible surface area have a great influence on the capacities. Theoretical capacity for LFP is 170 mAh g⁻¹ and at 0.5 C our composite sample B has a capacity of 164 mAh g⁻¹. This is accompanied by a capacity of still 109 mAh g⁻¹ at 10 C.

Since composites of active materials combined with porous carbons are of great interest for battery materials the scale up of such materials is important too. Most published materials, based on

ordered mesoporous carbons like CMK-3, are synthesized on a small scale with only several hundred milligrams of carbon. To gain access to larger amounts of carbon without having a very complicated or time/space consuming synthesis an EISA (evaporation induced self-assembly) based route with the implementation of polyurethane (PU) foam is an option [72].

An EISA process generally utilizes evaporation of a solvent (mostly ethanol). During this process a surfactant, for example pluronic F127 (triblock copolymer (EO₁₀₆PO₇₀EO₁₀₆)) and a precursor self-assemble. This is due to increasing interactions via hydrogen bonds during the evaporation of solvent. These interactions are leading to formation of micelles which are surrounded by the carbon precursor (phenolic resin) [13]. After complete solvent evaporation a thermopolymerization is applied, followed by carbonization. During this carbonization step the surfactant decomposes and a porous carbon is formed. A well-known carbon made with the EISA process is FDU-15. An EISA synthesis is normally done within laboratory equipment with a high surface to volume ratio as for example bowls, resulting in several micrometer thick polymer films (before carbonization). The PU foam is an alternative to the use of bowls. It has a three dimensional system of open pores, which dramatically increase the surface area. So

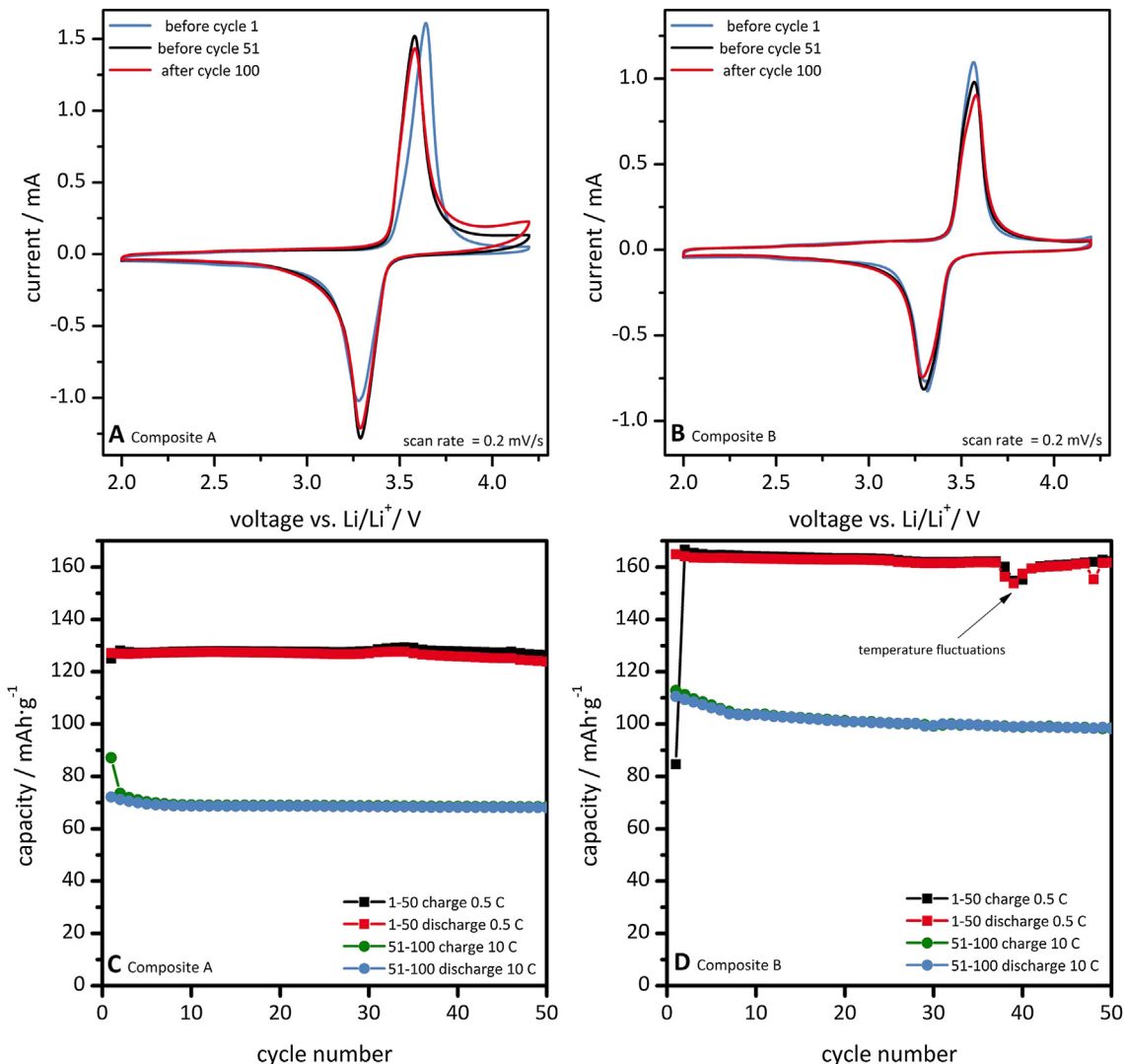


Fig. 15. Electrochemical performance of the composites A (left; A and C) and B (right; B and D). First 50 cycles are made with a C rate of 0.5 C and the cycles 51 to 100 are at 10 C. The CV experiments are measured at 0.2 mV s⁻¹. All experiments are done with 1 M LiPF₆ in EC/DMC 1:1 w/w.

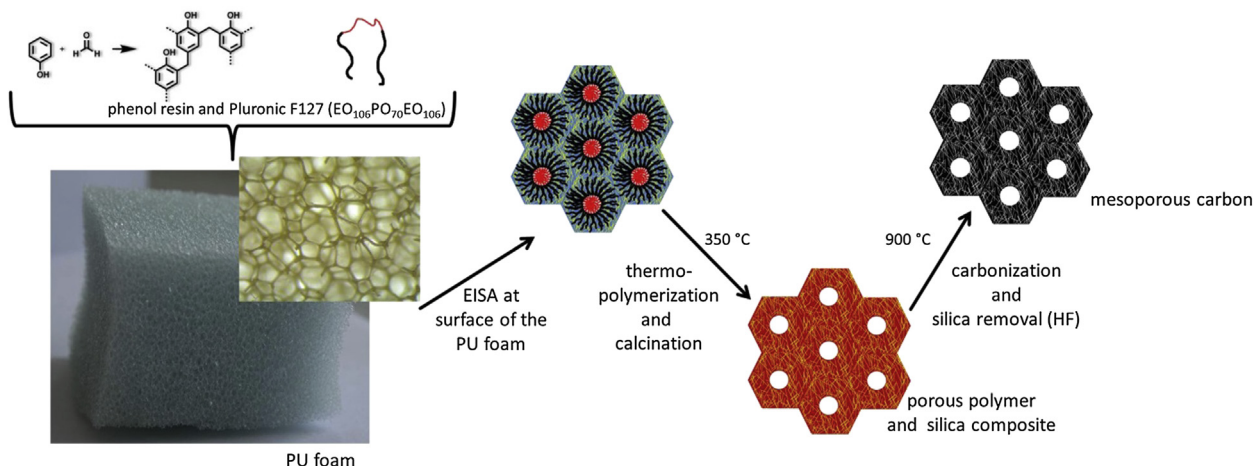


Fig. 16. Reaction scheme for the synthesis of porous carbons via EISA on PU foam.
Adapted with permission from the American Chemical Society [73].

instead of using more bowls for scaled up synthesis simply a third dimension is added, which reduces the laboratory space which is needed. In terms of pore volume and specific surface area FDU-15 ($650 \text{ m}^2 \text{ g}^{-1}$ and $0.37 \text{ cm}^2 \text{ g}^{-1}$) is behind CMK-3 ($1250 \text{ m}^2 \text{ g}^{-1}$ and $1.33 \text{ cm}^2 \text{ g}^{-1}$) [13]. To improve the pore volume and surface area of carbons made with the EISA process a synthesis introduced by Zhao and coworkers is used [73]. They added TEOS to reinforce the carbon structure and reduce pore shrinking during carbonization. This is due to formation of small (around 5 nm) silica particles during synthesis. Also it is not necessary to synthesize and characterize any hard template when an EISA process is used for porous materials synthesis. This reduces the time and costs needed for synthesis. A reaction scheme for the synthesis of the porous carbons with PU foam support is given in Fig. 16.

In Fig. 17 results from thermogravimetric analysis of two pure PU foams are shown, one in pure Ar atmosphere and one in synthetic air (Ar/O₂ 80:20). Both foams are decomposed when heated

Table 2

Summary of weight loss for PU foams in argon and argon/oxygen atmospheres.

Temperature	Weight loss Ar Atm.	Weight loss Ar/O ₂ Atm.
25–140 °C	0.74%	1.39%
140–350 °C	63.5%	71.5%
350–700 °C	35.6%	27.0%

above 240 °C. First weight loss can be assigned to loss of water, followed by full decomposition up to 700 °C (Table 2). The soft template F127 which is used in the EISA process does also undergo decomposition at 350 °C. This is a great synergetic effect, since no additional step is necessary. A heat treatment for 5 h at 350 °C

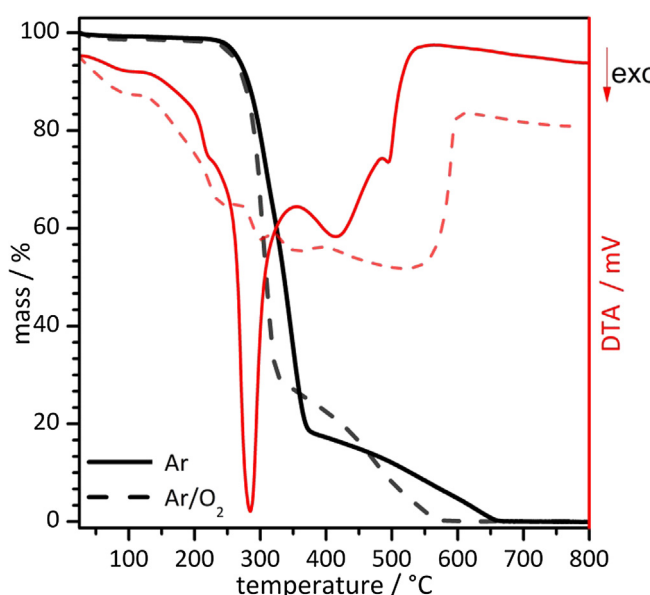


Fig. 17. TG (black) and DTA (red) measurements of PU foams in Ar (solid line) and Ar/O₂ (80:20; dashed line) atmospheres. Heating rate was 5 K min⁻¹ in both cases. (For interpretation of the references to color in this figure legend, the reader is referred to the web version of this article.)

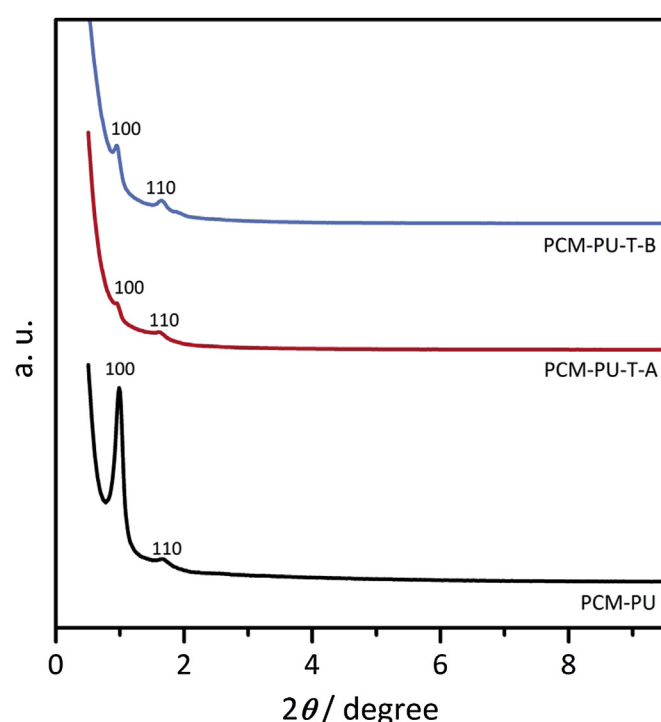


Fig. 18. X-ray diffraction patterns for carbons synthesized by using the EISA process in the pores of PU foams.

simply decomposes the PU foam and the surfactant F127. For preparation of highly porous carbons total decomposition of the support is mandatory, as any additional non porous material would decrease the specific surface area and pore volume.

Three different porous carbon materials with cylindrical pores were synthesized. F127 triblock copolymer is used as soft template and phenolic resin as carbon source. Common synthesis on PU foams using no additional TEOS is denoted as PCM-PU (PCM: porous carbon material). PCM-PU-T-A and PCM-PU-T-B are made with use of TEOS. The latter ones are varying in the ratio of phenolic resin to TEOS. For PCM-PU-T-B a higher amount of TEOS compared to resin (1:3 mol whereas PCM-PU-T-A has 1:1 mol) was used. Generally a phenol resin was made and dissolved into an F127/ethanol solution. Thermopolymerization was carried out in two steps at 100 °C and 160 °C followed by a carbonization at 900 °C for 2 h in Ar atmosphere for all three variations. The inorganic silica structures were subsequently removed by hydrofluoric acid.

X-ray diffraction patterns are shown in Fig. 18. A 2D-hexagonal scattering pattern is found for all three carbon materials. The positions of the (100) peaks show a shift in lattice constants for the three materials. This indicates differences in pore sizes or wall thickness. To further investigate the pore structure nitrogen sorption experiments are done. These measurements show typical isotherms of mesoporous materials with hysteresis between 0.4 and 0.6 p/p_0 (Fig. 19) for all three carbon materials.

The nitrogen physisorption data for all samples are shown in Table 3. The use of TEOS is increasing important characteristics like pore volume and specific surface area (BET) in the porous carbons. This is due to co-assembling of inorganic and organic precursor during synthesis, resulting in a very rigid polymer/silica composite [73]. The hydroxyl groups in both the resol and hydrolyzed TEOS can form hydrogen bonds. These improve the interactions between the EO groups of the soft template F127, organic resol and inorganic silicate materials. Under the applied acidic synthesis conditions, the inorganic phase condenses and therefore reinforces the carbon network. This has a direct influence to the pore size. Compared to the pure carbon both samples made with inorganic structure support have higher pore sizes (4.68 nm for PCM-PU, 4.84 nm for PCM-PU-T-A and 5.18 nm for PCM-PU-T-B), which is consistently with the X-ray diffraction patterns (Fig. 18). This is due to decreased

framework shrinkage during carbonization. More important than pore size gain is the change in pore volume and specific surface area (BET). The carbons made with TEOS have up to five times higher pore volumes. The synthesized porous carbon PCM-PU-T-B has nearly the same specific area and pore volume as previously used CMK-3 carbon as desired. Especially the raised pore volume is beneficial for a host material, since the amount of LFP, which can be loaded into the pores, is increased.

We again applied the *incipient wetness* method to fill the pores of the carbon with an LFP precursor solution. With the same reduction time (6 h) and temperature (650 °C) LFP was successfully synthesized in the pores of the carbon (see Fig. 20). After the synthesis of the LFP/carbon composite the reflexes originating from mesopores, which can be seen for the pure carbon (see inset Fig. 20), are no longer detectable. This indicates that the LFP was synthesized inside of the pores of the carbon.

Fig. 21 shows the corresponding nitrogen isotherms and pore size distributions. The composite has a much lower specific area of 441 $\text{m}^2 \text{ g}^{-1}$ (BET) and a lowered pore volume of 0.43 $\text{cm}^3 \text{ g}^{-1}$ compared to the pure carbon. This is another strong indication for the formation of the LFP phase inside of the pores of the carbon. Further electrochemical test are in preparation.

3.2. Porous lithium nickel manganese oxide

As $\text{LiNi}_{0.5}\text{Mn}_{1.5}\text{O}_{4-\delta}$ is a material of great interest because of its high capacity and potential, we also tested nanostructuring with this material (cf. Refs. [74,75]). To achieve this, we aimed at the synthesis of mesoporous $\text{LiNi}_{0.5}\text{Mn}_{1.5}\text{O}_{4-\delta}$ by various ways of exo-templating and carried out several analytical methods including powder X-ray diffraction (XRD), nitrogen physisorption, X-ray absorption near edge structure (XANES), inductively coupled plasma-atomic emission spectroscopy (ICP-OES), thermogravimetric analysis (TGA) and nuclear magnetic resonance (NMR) spectroscopy.

Mesoporous lithium nickel manganese oxide spinels ($\text{LiNi}_{0.5}\text{Mn}_{1.5}\text{O}_{4-\delta}$) were synthesized via the hard templating process. As templates SBA-15 or KIT-6 silica and CMK-3 or CMK-8 carbons were used. Properties of the templates according to the pore structure received by nitrogen physisorption are shown in Table 4.

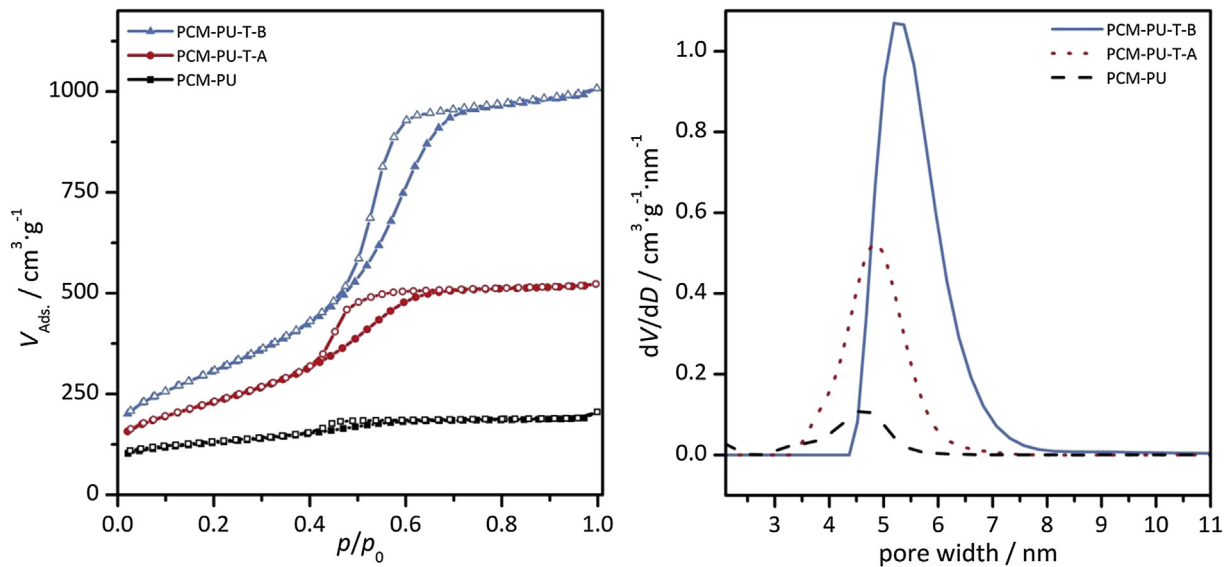


Fig. 19. Nitrogen physisorption isotherms (77 K; filled symbols: adsorption; empty symbols: desorption) of porous carbons made with PU foam support. On the left side the isotherms are displayed. Pore size distribution of the samples on the right side are calculated using QSDFT method (desorption branch, cylindrical pores).

Table 3

Summary of nitrogen sorption data analysis for the porous carbon made on PU foam and the corresponding composites.

Sample	TEOS/mmol	$S_{\text{BET}}/\text{m}^2 \text{ g}^{-1}$	Pore size/nm	Pore volume/cm $^3 \text{ g}^{-1}$
PCM-PU	—	462	4.68	0.28
PCM-PU-T-A	1	829	4.84	0.77
PCM-PU-T-B	3	1136	5.18	1.47
LFP@PCM-PU-T-B	—	441	5.01	0.43

The synthesis procedure of the mesoporous spinel differed depending on the applied template (carbon or silica) due to their different stabilities during heat treatment. If a carbon template is used, the temperature for thermal conversion in air cannot exceed

450 °C because otherwise the pore structure of the metal oxide will collapse due to the early decomposition of the template. The conversion of pure $\text{LiNi}_{0.5}\text{Mn}_{1.5}\text{O}_{4-\delta}$ precursors at 450 °C will not yield any crystalline phase of the spinel (Fig. 22). However, a crystalline phase of spinel formed even at temperatures of 250 °C when a carbon template was used (here CMK-8). As can be seen by the XRD patterns a heat treatment of the precursor and carbon template composite at 450 °C yielded an increase of crystallinity and furthermore only a pure $\text{LiNi}_{0.5}\text{Mn}_{1.5}\text{O}_{4-\delta}$ phase was obtained (Fig. 22).

Type IV isotherms recorded by nitrogen physisorption show typical H1 hysteresis, which are characteristic of mesoporous materials (Fig. 23). As expected, the uptake of nitrogen is decreased by

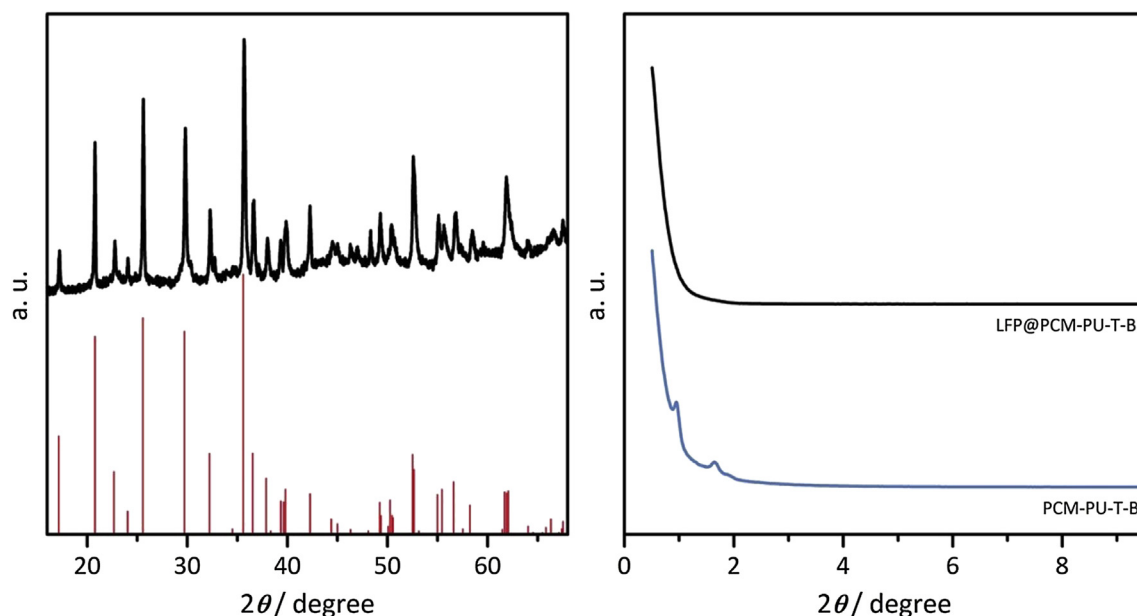


Fig. 20. X-ray diffraction pattern of LFP synthesized inside of the pores of PCM-PU-T-B. The red bars show the comparison pattern of LFP (PDF-01-083-2092). On the right side the small angle X-ray diffraction pattern of the porous carbon PCM-PU-T-B (blue) and the composite (black) is shown. (For interpretation of the references to color in this figure legend, the reader is referred to the web version of this article.)

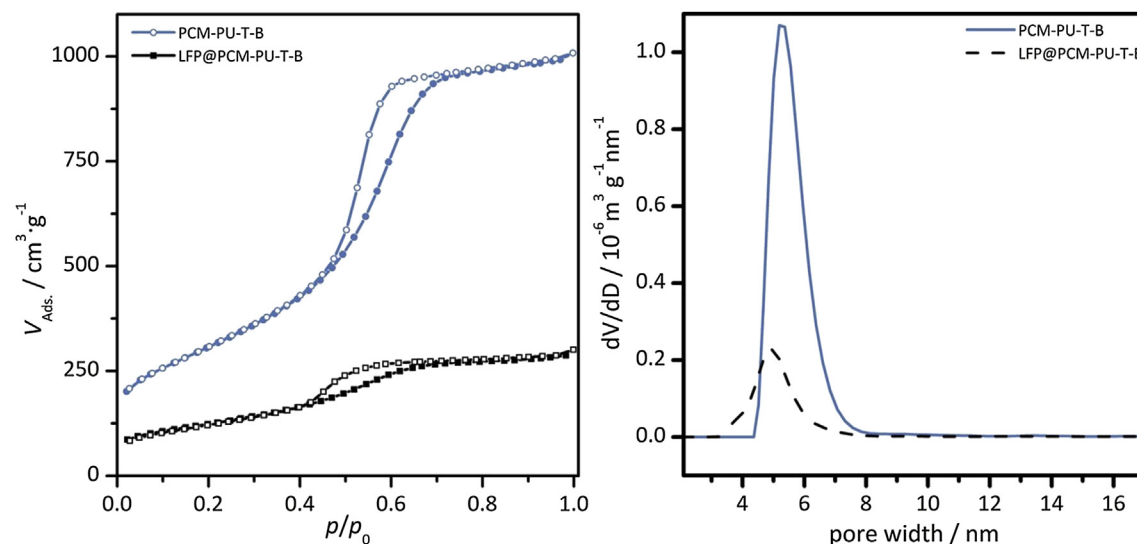


Fig. 21. Nitrogen physisorption isotherms (77 K; filled symbols: adsorption; empty symbols: desorption) of porous carbon (blue) and corresponding LFP/C composite (black). Pore size distribution of the samples are displayed on the right (QSDFT analysis of desorption branch, cylindrical pores). (For interpretation of the references to color in this figure legend, the reader is referred to the web version of this article.)

Table 4

Summary of nitrogen physisorption data analysis for the applied carbon and silica templates.

Template	$S_{\text{BET}}/\text{m}^2 \text{ g}^{-1}$	Pore size/nm	Pore volume/cm $^3 \text{ g}^{-1}$
SBA-15 silica	561	9.8	1.28
KIT-6 silica	552	10.9	1.50
CMK-3 carbon	1153	4.8	1.65
CMK-8 carbon	1008	4.7	1.53

filling the pores with the preformed $\text{LiNi}_{0.5}\text{Mn}_{1.5}\text{O}_{4-\delta}$. Since one part of the remaining surface area after filling the pores and heat treatment at 250 °C arises from the template, the uptake of nitrogen is decreased again after removal of the template. For the porous $\text{LiNi}_{0.5}\text{Mn}_{1.5}\text{O}_{4-\delta}$ a surface area of 62 $\text{m}^2 \text{ g}^{-1}$ is detected. The analysis of the physisorption data is summarized in Table 5.

Cycling experiments of this porous $\text{LiNi}_{0.5}\text{Mn}_{1.5}\text{O}_{4-\delta}$ (0.3 C, 2.9–5.0 V) show low initial capacity of about 100 mAh g^{-1} and significant capacity fading of about 93% in the first 20 cycles (Fig. 24).

To directly observe the degradation of the cathode material a similarly performing material casted from CMK-3 was examined. The distribution of manganese species after 53 cycles running from 3.9 to 5.0 V with 0.5 C rate (electrolyte EC/DMC 1:1 w/w) was investigated by confocal micro-X-ray fluorescence (CMXRF) combined with XANES at the Mn–K edge [76]. By the mentioned technique, oxidation states of manganese can be determined at different depths of the electrode, providing a better insight into the cathode surface reactions. It was found that the oxidation state of manganese differs significantly before and after cycling and also depends on the measurement depth. Analysis of a non-cycled electrode showed an average oxidation state of +3.79 for manganese through the entire depth of the sample. After cycling a gradient of oxidation state could be observed. At the surface of the

cathode an oxidation state of +4.0 was determined, while in depth the value reached only +3.73, dropping steadily. The oxidation state of +4.0 at the cathode surface suggests that the present phase might be MnO_2 , as assumed by Aurbach et al. [77]. Contrary to this result the EXAFS region of the spectrum of the tested sample shows oscillations fitting to the spectrum of $\text{LiNi}_{0.5}\text{Mn}_{1.5}\text{O}_{4-\delta}$ in $P43212$ structure ($\delta = 0$) and not to MnO_2 (Fig. 25) [76]. Nevertheless, the increase of oxidation state indicates the degradation of the active material. An oxidation state gradient observed during in-depth analysis of the cathode layer illustrates that a surface reaction takes place and the disproportionation reaction of Mn^{3+} into Mn^{2+} and Mn^{4+} , accompanied by Mn^{2+} dissolution is promoted by the electrolyte. In comparison to the cycled bulk $\text{LiNi}_{0.5}\text{Mn}_{1.5}\text{O}_{4-\delta}$, the degradation, based on the oxidation state, is about 60% higher for mesoporous material.

Mesoporous $\text{LiNi}_{0.5}\text{Mn}_{1.5}\text{O}_{4-\delta}$ could also be synthesized by application of a silica hard template (here SBA-15 silica). This offers the possibility of higher synthesis temperatures, leading to a higher crystallinity, and overcomes the problems of electrochemical performance low crystallinity is attributed to.

To figure out the proper synthesis temperature of $\text{LiNi}_{0.5}\text{Mn}_{1.5}\text{O}_{4-\delta}$ in a silica matrix a sequence of heat treatments was performed (Fig. 25). It is obvious that at a temperature of 700 °C and higher a single phase and a sufficient crystallinity is reached. Below this temperature the peaks were very weak and broad, which indicates small crystallite sizes. Peak broadening of the template spinel compared to the bulk material occurs because of the small dimensions of the pores, which allow only smaller crystal domains to grow. However, the temperature must not be too high because otherwise lithium can react with the silica to form quartz or lithium silicates as it is the case at 800 °C (Fig. 27). These byproducts render the material useless because of their insolubility in virtually any solvent.

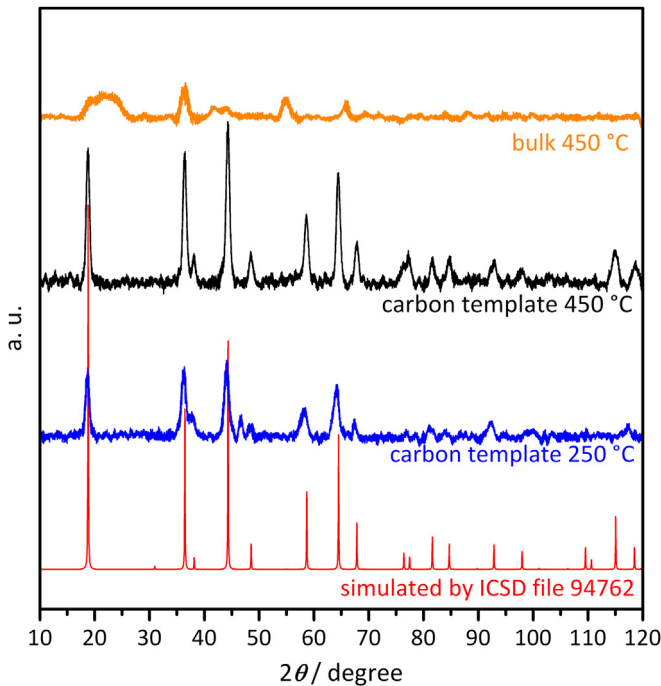


Fig. 22. Powder X-ray diffraction patterns of different $\text{LiNi}_{0.5}\text{Mn}_{1.5}\text{O}_{4-\delta}$ batches. Black line: $\text{LiNi}_{0.5}\text{Mn}_{1.5}\text{O}_{4-\delta}$ made from carbon matrix (CMK-8) at 450 °C. Blue line: $\text{LiNi}_{0.5}\text{Mn}_{1.5}\text{O}_{4-\delta}$ made from carbon matrix (CMK-8) at 250 °C. Orange line: bulk $\text{LiNi}_{0.5}\text{Mn}_{1.5}\text{O}_{4-\delta}$ converted at 450 °C. Red line: simulated P-XRD pattern of $\text{LiNi}_{0.5}\text{Mn}_{1.5}\text{O}_{4-\delta}$ (ICSD 94762). (For interpretation of the references to color in this figure legend, the reader is referred to the web version of this article.)

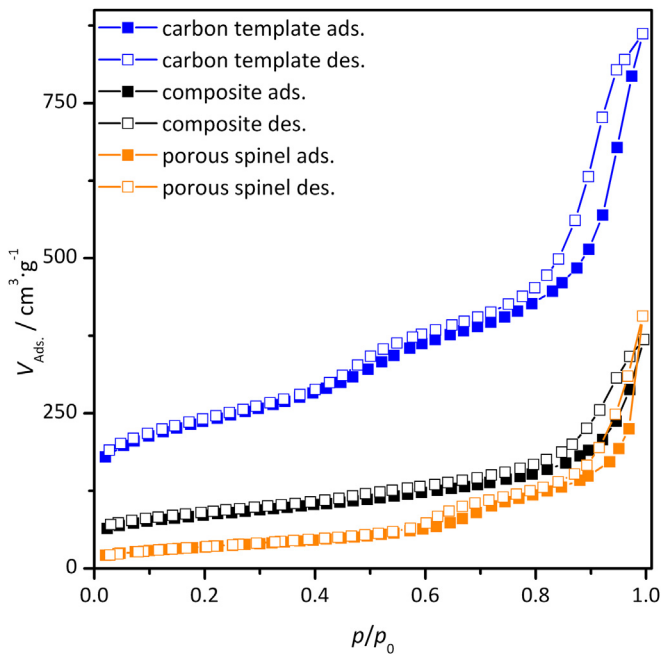


Fig. 23. Nitrogen physisorption isotherms (77 K; filled symbols: adsorption; empty symbols: desorption) of the carbon template CMK-8 (blue), the composite of the preformed $\text{LiNi}_{0.5}\text{Mn}_{1.5}\text{O}_{4-\delta}$ in the carbon template (black) and the porous spinel $\text{LiNi}_{0.5}\text{Mn}_{1.5}\text{O}_{4-\delta}$ after the removal of the template (orange). (For interpretation of the references to color in this figure legend, the reader is referred to the web version of this article.)

Table 5

Summary of nitrogen physisorption data analysis for the carbon preformed- $\text{LiNi}_{0.5}\text{Mn}_{1.5}\text{O}_{4-\delta}$ composite and the porous spinel.

Material	$S_{\text{BET}}/\text{m}^2 \text{ g}^{-1}$	Pore size/nm	Pore volume/cm $^3 \text{ g}^{-1}$
Composite carbon-spinel	306	Undefined	0.31
Porous spinel	62	4.4	0.21

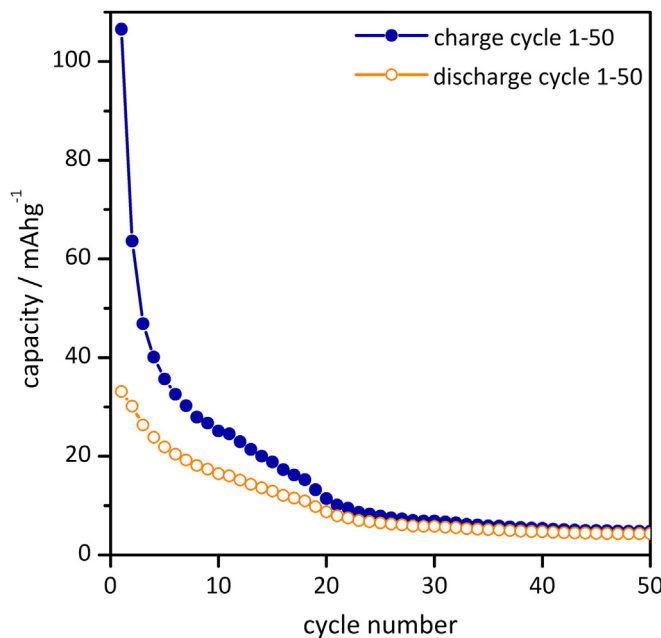


Fig. 24. Cycling experiment of mesoporous spinel $\text{LiNi}_{0.5}\text{Mn}_{1.5}\text{O}_{4-\delta}$ casted from carbon template CMK-8. Cycled with 0.3 C at room temperature in a potential range of 3.8–4.9 V. Using 1 M LiPF_6 in EC/DMC 1:1 w/w as electrolyte. Charge (blue filled symbols) and discharge capacities (orange empty symbols) were recorded. (For interpretation of the references to color in this figure legend, the reader is referred to the web version of this article.)

Subsequent dissolution of the hard template yielded in mesoporous spinel with a surface area of $178 \text{ m}^2 \text{ g}^{-1}$. The type IV isotherms recorded by nitrogen physisorption show H1 hysteresis typical for mesoporous materials (Fig. 28). By filling the pores of the template with the spinel the nitrogen uptake decreased strongly

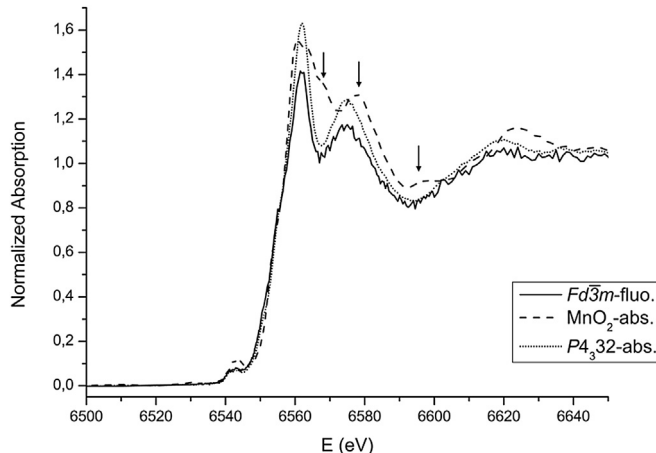


Fig. 25. Comparison of absorption XANES measurements of the MnO_2 standard and the spinel with $\text{P}4_3\text{2}$ structure with the surface of the cycled bulk $\text{Fd}3\text{m}$ spinel cathode material, different oscillations are indicated with arrows. Reproduced with permission of Elsevier [76].

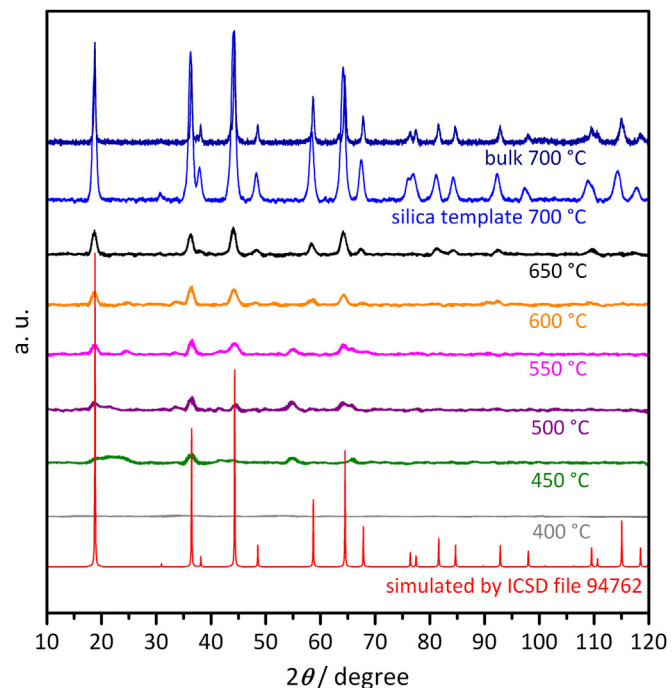


Fig. 26. Powder X-ray diffraction patterns of $\text{LiNi}_{0.5}\text{Mn}_{1.5}\text{O}_{4-\delta}$ synthesized in a silica matrix (SBA-15) at different temperatures. Dark blue: bulk $\text{LiNi}_{0.5}\text{Mn}_{1.5}\text{O}_{4-\delta}$ synthesized at 700 °C. Red line: simulated P-XRD pattern of $\text{LiNi}_{0.5}\text{Mn}_{1.5}\text{O}_{4-\delta}$ (ICSD 94762). (For interpretation of the references to color in this figure legend, the reader is referred to the web version of this article.)

because the pores are blocked. After dissolution of the template the porosity increased again arising from the now free standing network of the porous spinel. Analysis of the sorption data is summarized in Table 6.

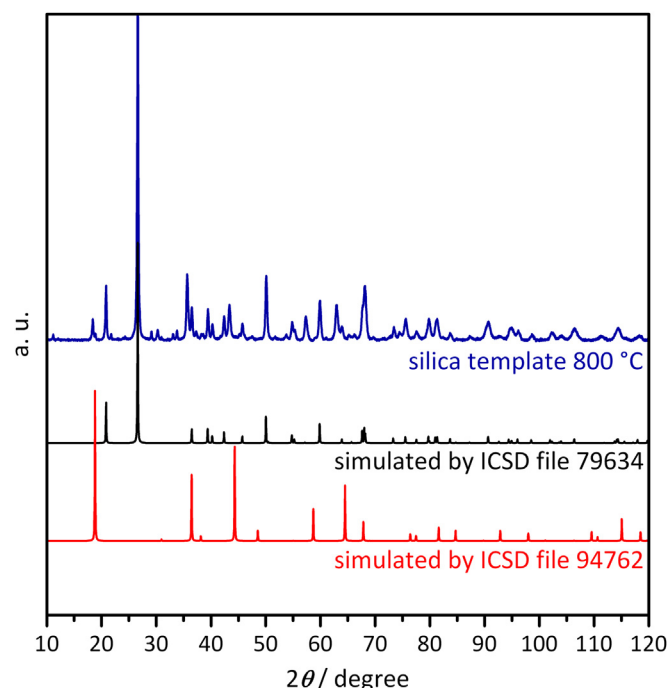


Fig. 27. Powder X-ray diffraction patterns of $\text{LiNi}_{0.5}\text{Mn}_{1.5}\text{O}_{4-\delta}$ synthesized in a silica matrix (SBA-15) at 800 °C. Black line: simulated P-XRD pattern of quartz (ICSD 79634). Red line: simulated P-XRD pattern of $\text{LiNi}_{0.5}\text{Mn}_{1.5}\text{O}_{4-\delta}$ (ICSD 94762). (For interpretation of the references to color in this figure legend, the reader is referred to the web version of this article.)

ICP-OES measurements showed no significant amount of silicon and a molar ratio of $\text{Li}_{0.6}\text{Ni}_{0.5}\text{Mn}_{1.22}\text{O}_{2.64}$. The value of the oxygen ratio is calculated by the experimental data for the metal ions and hence not considering any deficiency of oxygen. The loss of lithium might be caused by insertion of lithium into the silica template. Hence, by dissolution of the template the lithium ions inserted to the template structure will be washed out too.

Another useful method to make statements about crystallinity and the phase of the obtained spinel is ^7Li NMR spectroscopy. The spectrum provides information about the local ordering and site occupancy of lithium cations (Fig. 29). Isotropic resonance at approximately 900 ppm indicates that lithium cations are located in tetrahedral sites of $\text{LiNi}_{0.5}\text{Mn}_{1.5}\text{O}_{4-\delta}$, surrounded by Ni^{2+} and high oxidation state of Mn of about +3.9 [78]. This shows that $\text{LiNi}_{0.5}\text{Mn}_{1.5}\text{O}_{4-\delta}$ is built in the $\text{Fd}\bar{3}m$ space group.

Due to the elevated synthesis temperature the crystallinity was increased and formation of the desired phase was promoted as one can see by XRD and NMR spectrum (Figs. 26 and 29). First electrochemical cycling experiments led to an initial capacity of about 109 mAh g⁻¹ (Fig. 30) with a capacity retention of 24% after 150 cycles. The cyclic voltammogram shows typical peaks for $\text{LiNi}_{0.5}\text{Mn}_{1.5}\text{O}_4$ in $\text{Fd}\bar{3}m$ structure including the oxidation peak at about 4 V representing the oxidation of Mn^{3+} to Mn^{4+} and two oxidation peaks at 4.7 V generated by the process of Ni^{2+} converted to Ni^{4+} (Fig. 31).

Mechanisms for capacity fading have been proposed by Yue and coworkers [79]. For samples decomposed while cycling at 60 °C a disintegration of microparticles into nanoparticles was observed by SEM images. This leads to a reduced contact between active material and current collector. Furthermore, high surface areas of porous compounds offer a great potential for side reactions with the electrolyte. The high voltage for the redox reaction of nickel leads in general to decomposition of commercial electrolytes accompanied by a dissolution of nickel and manganese from the active material. A proposed reaction mechanism, supported by the

Table 6

Summary of nitrogen physisorption data analysis for the silica- $\text{LiNi}_{0.5}\text{Mn}_{1.5}\text{O}_{4-\delta}$ composite and the porous spinel.

Material	$S_{\text{BET}}/\text{m}^2 \text{ g}^{-1}$	Pore size/nm	Pore volume/cm ³ g ⁻¹
Composite silica-spinel	86	6.0	0.14
Porous spinel	178	6.6	0.30

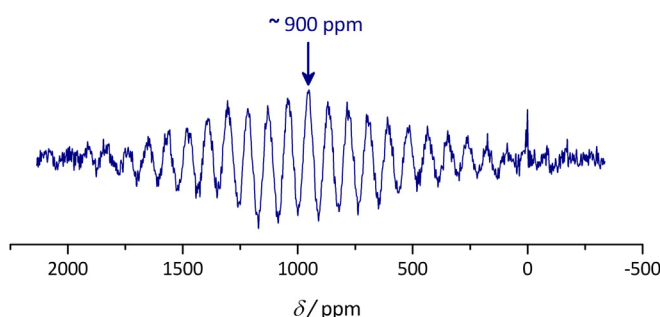
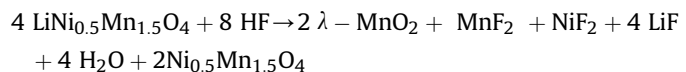


Fig. 29. ^7Li MAS NMR of mesoporous spinel casted from silica template at 700 °C. The isotropic resonance is denoted with an arrow. The other signals are spinning sidebands.

appearance of lithium and fluorine in increased concentrations on the cathode surface is the following: [79]



Concentrations were determined by XPS measurements in comparison to pristine material.

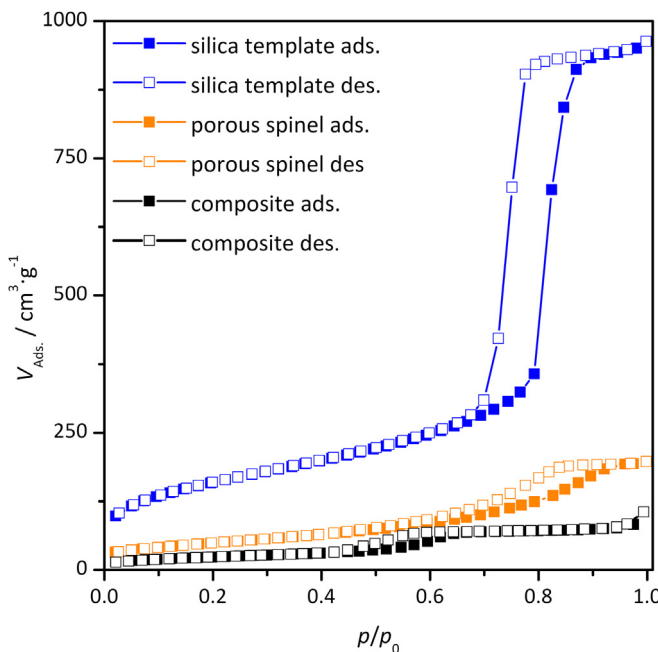


Fig. 28. Nitrogen physisorption isotherms (77 K; filled symbols: adsorption; empty symbols: desorption) of the silica template KIT-6 (blue), the composite of $\text{LiNi}_{0.5}\text{Mn}_{1.5}\text{O}_{4-\delta}$ in the silica template (black) and the porous spinel $\text{LiNi}_{0.5}\text{Mn}_{1.5}\text{O}_{4-\delta}$ after the removal of the template (orange). Filled symbols denote adsorption, empty symbols denote desorption. (For interpretation of the references to color in this figure legend, the reader is referred to the web version of this article.)

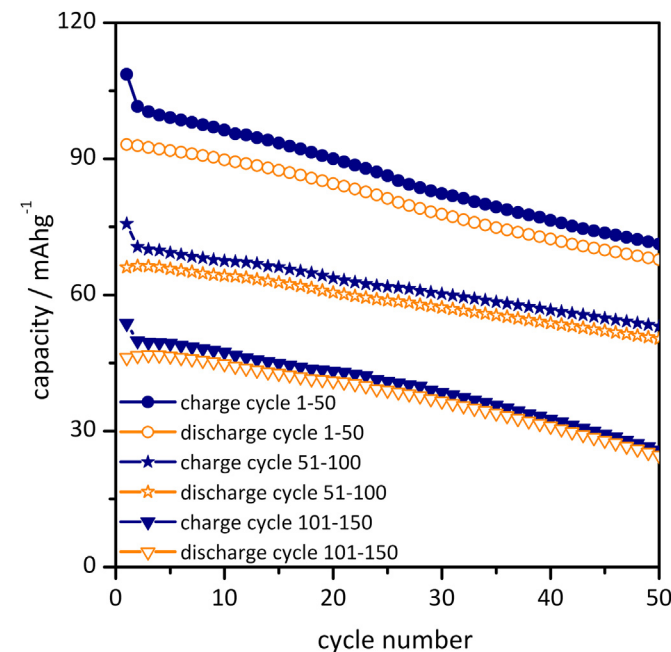


Fig. 30. Cycling experiment of mesoporous spinel casted from silica template KIT-6 with 0.3 C at room temperature in a potential range of 3.8–4.9 V. 1 M LiPF_6 in EC/DMC 1:1 w/w served as electrolyte. Charge (blue filled symbols) and discharge (orange empty symbols) capacities were recorded. After every 50th cycle a CV was recorded (Fig. 31). (For interpretation of the references to color in this figure legend, the reader is referred to the web version of this article.)

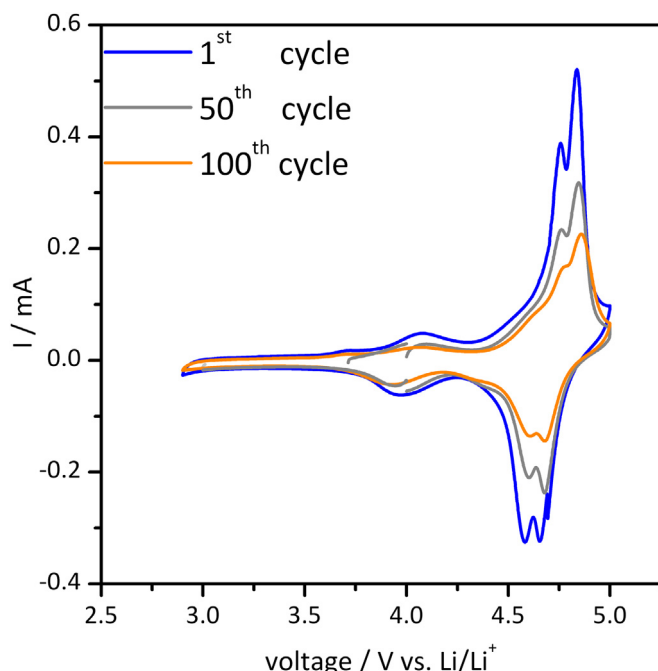


Fig. 31. Cyclovoltammogram (CV) for the 1st (blue), the 50th (gray) and the 100th (orange) cycle of mesoporous spinel casted by silica template KIT-6. A scan rate of 0.1 mV s^{-1} was applied. 1 M LiPF₆ in EC/DMC 1:1 w/w served as electrolyte. (For interpretation of the references to color in this figure legend, the reader is referred to the web version of this article.)

3.3. Lithium nickel manganese oxide thin film model system

Verification that the deposited films consist of the desired LNMO spinel phase was achieved by cyclic voltammetry due to characteristic peaks and by XRD (not shown here). Despite the use of an oxygen background gas during LNMO deposition, in order to maintain the oxygen stoichiometry of the spinel, a small oxygen deficit is established as revealed by the presence of a peak at 4.0 V vs. Li/Li⁺ in the cyclic voltammetry (CV) measurements as depicted in Fig. 32. It results from the oxidation of trivalent to tetravalent manganese ions during charging. Mn⁴⁺ ions are only present in the structure if an oxygen deficit exists in the spinel. Despite the fact that Mn³⁺ shows Jahn-Teller deformation, resulting in a decreased structural stability, small amounts of these

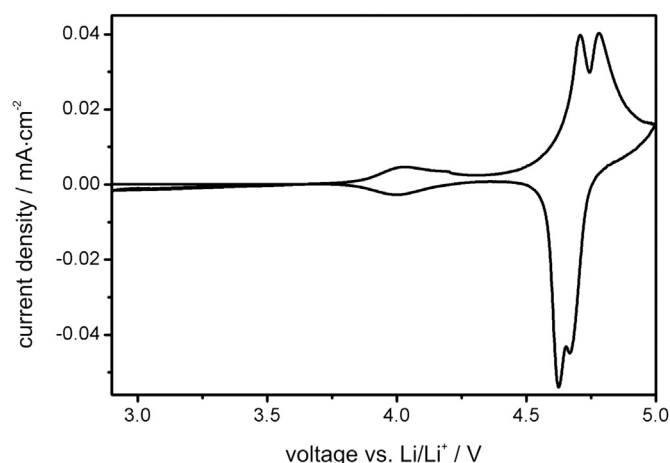


Fig. 32. Cyclovoltammogram (CV) of an LNMO thin film on a Pt–YSZ substrate cycled with 1 M LiPF₆ in EC/DMC 1:1 w/w as electrolyte and lithium foil as counter electrode. A scan rate of 0.1 mV/s was applied.

ions are beneficial for electronic conductivity. Thus, better electrochemical performance is reached using LNMO with a small oxygen deficit which also causes a change in crystal structure from $P4_332$ for the oxygen stoichiometric spinel to $Fd\bar{3}m$ for the deficit one. LNMO deposition needs high temperatures of 950–1000 °C to deliver sufficient flat films, with a roughness of less than 10 nm. Moreover, scanning electron microscope (SEM) images in Fig. 33 reveal a cubic spinel structure with an orientation along the (100) axis.

As already shown in Fig. 32 the CV of an LNMO thin film shows a small peak in the range of 4.0 V vs. Li/Li⁺ caused by the oxidation of residual trivalent manganese in the spinel structure. The main electrochemical activity takes place between 4.6 V and 4.8 V where Mn²⁺ is oxidized to Mn⁴⁺. Therefore, the thin film shows the same features like technical LNMO electrodes with a small oxygen deficit and is suitable as model system since the main reactions are located in the same voltage range and no side reactions are visible. However, one has to keep in mind that the dimensions of the active material particles in technical electrodes and the dimension of the thin film are completely different. Thus, other reactions may become rate determining and the resulting surface film may vary. But, as we will show in the following section, a comparison to CEI investigations on technical LNMO and LiMn₂O₄

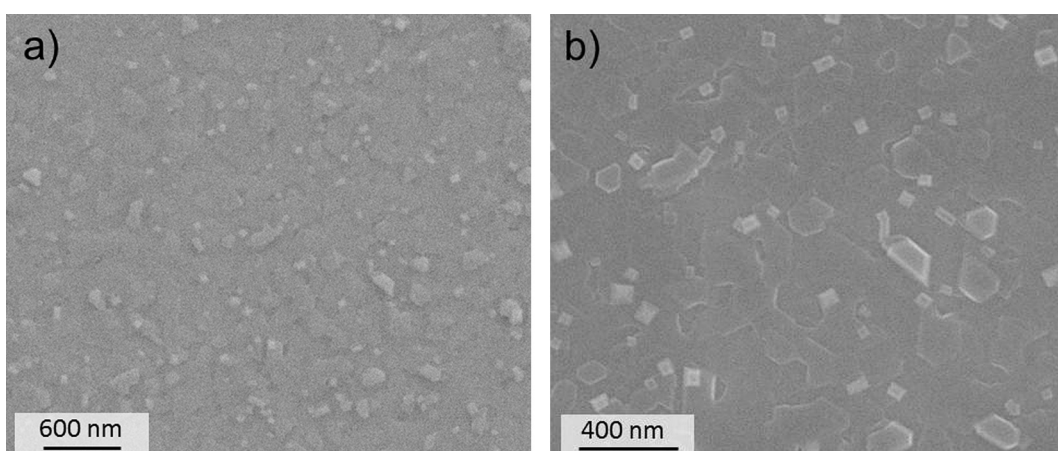


Fig. 33. SEM images of an LNMO thin film deposited on a Pt–YSZ substrate. a) overview, b) higher magnification showing the cubic structure of the layer.

electrodes by the groups of Aurbach and Edström deliver the same main composition, so that at least the main features of the surface film formation are well comparable using the thin film model approach [77,80].

In Fig. 34 charge and discharge capacities of an LNMO thin film are shown. Obviously, there is a large irreversible capacity in the first three cycles. Afterward, it reduces to a small, constant value, showing that in the beginning of the cycling side reactions occur to a large extent, presumably leading to the formation of a stable interfacial film between electrode and electrolyte. Once this is established only small electrolyte oxidation occurs and the capacity of the film remains nearly stable. However, this behavior does not hold for all investigated LNMO thin film electrodes and sometimes the capacity keeps on fading. Up to now, we have no explanation for this different behavior, but we assume that the cell assembling has a large impact on the behavior as the overall active mass is very small. Therefore, surface reactions caused by imperfect cell setup are more important than in technical electrodes where only a small percentage of the active material is located at the surface.

As surface film formation takes place on both electrodes, the observed irreversible capacity could also contain some contribution of the SEI formation on the anode. However, due to its "intrinsic potential" of 3.1 V vs. the standard hydrogen electrode, an interphase forms instantaneously on metallic lithium upon electrolyte contact since almost no solvent or salt is thermodynamically stable under these conditions [81]. Therefore we can assume, that the main part of the observed irreversible capacity results from the film formation on the cathode. There is an additional hint to the film formation as the first cycle is obviously different to the following ones as a peak at about 4.2 V vs. Li/Li⁺, which is clearly visible in the differential capacity plot in Fig. 35 (marked with a red arrow, in the web version), disappears later on.

SIMS depth profiles were performed in the negative investigation modus in which only negatively charged ions are detected. Metal oxides deliver a higher count rate in the negative detection mode compared to the pure metal. In the positive mode, in which metals deliver higher count rates, the lithium signal reaches too many counts to be detected correctly.

Fig. 35 shows a comparison between the SIMS depth profiles of a fresh and a cycled LNMO thin film electrode using the MnO[−] signal. This ion was chosen as indicator for the cathode material,

as manganese is besides oxygen the main element in the spinel and its content should be roughly the same in all investigated samples. For the fresh LNMO thin film the MnO[−] signal shows a steep rise in the beginning of the depth profile and remains constant afterward over the whole investigated range. For the cycled LNMO thin film we observe an increase of the MnO[−] signal over a broader range, and a constant value of almost the same height as for the fresh one is reached in deeper regions, which correlates with the MnO[−] volume value of the spinel. The slow rise of the latter signal indicates that the LNMO electrode has an about 50 nm thick surface layer after cycling. Indeed, other ions show an enrichment in this region of the SIMS depth profile in which the MnO[−] signal is lowered.

In Fig. 36 profiles of the C₃ signal of a fresh and a cycled LNMO electrode are exemplarily shown. Whereas for the uncycled sample the intensity decreases steeply, there is a clear enrichment for the cycled one, showing that this species is accumulated in the surface film on the cathode. The same trend is observable for a variety of other both organic and inorganic species. Additionally, it becomes clear that the maxima of the different species, indicating their highest enrichment, are at slightly different positions (Fig. 37). Thus, we propose a stacked setup of the CEI where fluorine containing species are found on the electrolyte side of this interfacial film, presumably caused by decomposition of the electrolyte salt LiPF₆. Thereafter mainly organic, partially polymeric species are found which are followed by lithium containing ones like lithium carbonate. Subsequent to this layer, inorganic species like phosphorus oxides are found, and closest to the cathode reaction products between the transition metals from the LNMO and electrolyte species like MnF₂ which itself is solvable in electrolyte are formed. This stacked structure was also reported for the SEI on lithium or graphite anodes containing of a thick and porous organic layer on the electrolyte side and an inorganic one located close to the electrode surface [82,83]. The dissolution of nickel is under discussion, and our results support this theory. A stacked setup of the CEI was also reported by the group of Edström and LiF, C–F and P–F_x species as CEI components are described in accordance with the studies by Aurbach et al. [77,82].

Cycling at higher temperatures (60 °C) for the same number of cycles results in a surface layer of the same composition but with increased thickness as also reported by Edström et al. who

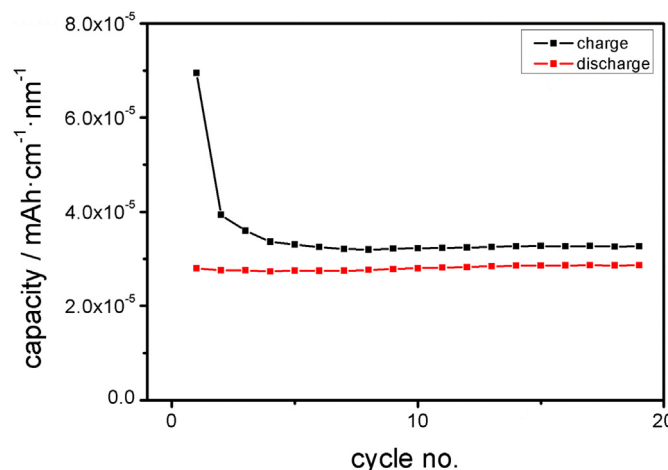


Fig. 34. Charge and discharge capacities of the first twelve cycles of a pouch cell comprising an LNMO thin film and lithium foil as working and counter electrode, respectively. 1 M LiPF₆ in EC/DMC 1:1 w/w was used as electrolyte and cycling was performed with a constant current of 8.1 μA, which equates to roughly 2.5 C. Capacity was normed to film volume and not like common to weight of the active mass since so few amount was deposited that it could not be weight.

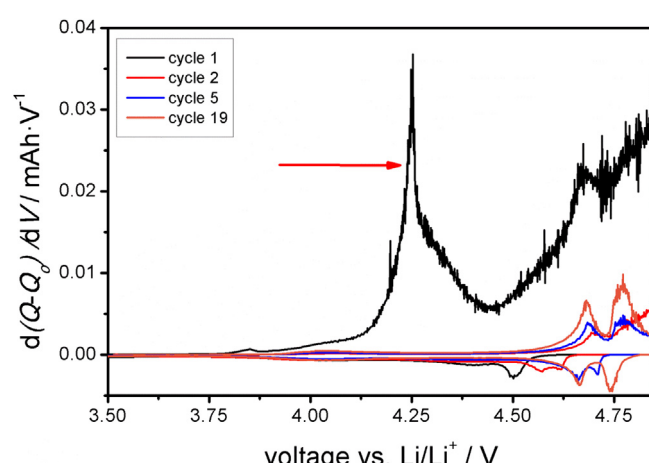


Fig. 35. Differential capacity of the 1st, 2nd, 5th and 19th cycle of a pouch cell comprising an LNMO thin film and lithium foil as working and counter electrode, respectively. 1 M LiPF₆ in EC/DMC 1:1 w/w was used as electrolyte and cycling was performed with a constant current of 2.0 μA, which equates to roughly 0.5 C. The arrow denotes the irreversible capacity only visible in the first cycle.

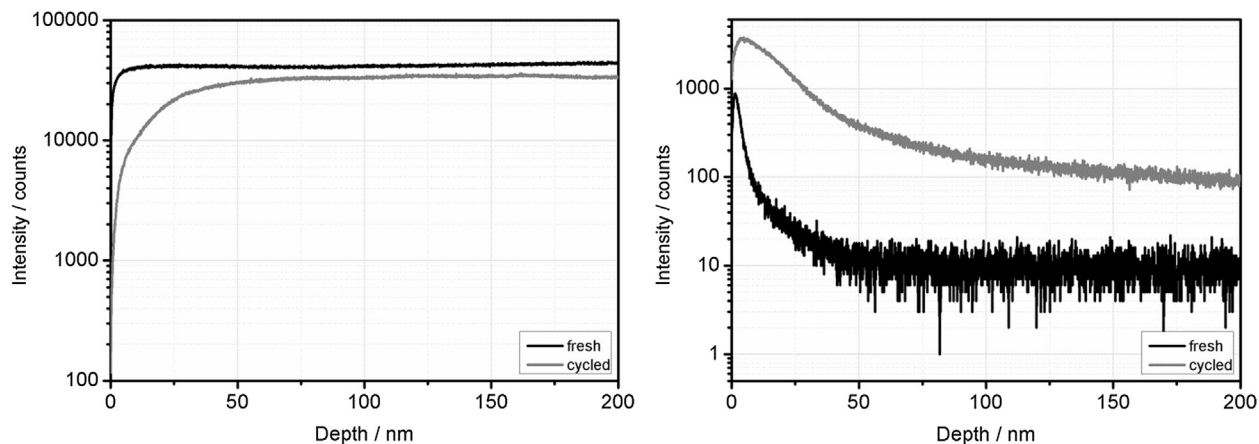


Fig. 36. SIMS depth profiles of MnO^- species on the left and C_3^- species on the right. Each showing the comparison between a fresh and a cycled LNMO thin film electrode.

investigated technical LiMn_2O_4 spinel electrodes by XPS [80]. There are also hints that surface film formation already takes place during the storage of the LNMO thin films assembled in a cell. The composition is the same as found after cycling, but only short chained polymers could be detected. However, storage in pure electrolyte for the same time also results in a thin surface film, but it lacks of PO_x and polymeric species. Thus, we can conclude that the presence of an electrical potential is necessary to establish a surface film of the composition reported previously. In contrast to this, Edström et al. report nearly identical surface films for both electrochemical cycled and stored films. A minimal difference between both treatments arises from the fact that the kinetics for surface film formation may be more favorable during cycling due to enhanced mass transport in the electrolyte [80,82].

In conclusion, SIMS investigations of the surface layer formed on LNMO thin films reproduce well the results for technical electrodes and allow an estimation of the CEI thickness to roughly 50 nm. However, some questions remain concerning the stability of the formed surface film like e.g.: Does it really stick to the surface or is it just attached to it due to close contact between the separator and

the electrode so that normally solvable decomposition products could not be transported away? Is the CEI really dense (like the SEI on the anode) and does it protect the electrode after its establishment for further reaction with the electrolyte? These questions cannot be answered solely by SIMS investigations, so that additional investigation methods like detailed impedance spectroscopy or a modified cell setup without separator and excess electrolyte to enable solvable products to be washed away are needed to complete the picture of the surface film formed on the cathode in lithium ion batteries.

4. Conclusion

We could demonstrate that it is possible to synthesize composites of pure LFP in good crystallinity with different types of mesoporous carbons. The obtained composites have a high capacity of 164 mAh g^{-1} and show a good performance in cycling tests. For future use as active material we successfully demonstrated use of a simple synthesis for scale up of mesoporous carbons with great specific surface areas and high pore volumes. Furthermore a successful conversion to LFP containing composites is shown. This will allow to easily adjust the carbon matrix to the specific properties needed for the active material.

Mesoporous $\text{LiNi}_{0.5}\text{Mn}_{1.5}\text{O}_{4-\delta}$ spinel was synthesized using different hard templates. Syntheses in carbon matrices were possible at low conversion temperatures but the resulting active material shows an electrochemical poor performance. Nevertheless XANES experiments allowed first conclusions on the surface chemistry of mesoporous spinel as cathode material, which showed the decrease of oxidation state of manganese dependent on depth of cathode layer and the transformation from disordered to ordered spinel. Using a silica matrix (KIT-6) as hard template made a synthesis of mesoporous $\text{LiNi}_{0.5}\text{Mn}_{1.5}\text{O}_{4-\delta}$ in $Fd\bar{3}m$ structure with a surface area of $178 \text{ m}^2 \text{ g}^{-1}$ possible. Crystallinity and phase pureness were approved by XRD and NMR techniques. First cycling experiments showed an initial capacity of 109 mAh g^{-1} with capacity retention of 24% after 150 cycles.

A thin film model for LNMO cathode materials was successfully established and with it we were able to investigate the constitution of the cathode electrolyte interface (CEI). These findings can be used in the future to optimize electrode surfaces as also electrolyte compositions.

The presented materials and their electrochemical characterizations do show that optimization needs to take the nanostructure into account. Further studies on model systems as on active

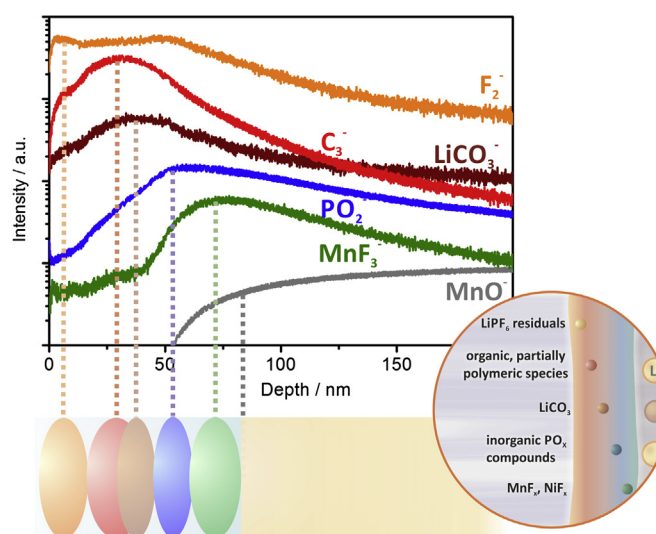


Fig. 37. SIMS depth profile of selected ions of a cycled LNMO electrode showing the stacked setup of the CEI. For better visibility all ions were normalized to the same bulk value at a depth of approx. 120 nm. The inset shows a schematic sketch of the CEI setup as indicated by our SIMS measurements.

materials are necessary to determine the impact of nanostructures as porosity or grain boundaries on electrode processes like oxidation or lithium diffusion.

Acknowledgments

This work was supported by the German Research Foundation (Deutsche Forschungsgemeinschaft, DFG) within the coordinated program “Materials for lithium ion high performance batteries” (projects FR 1372/15-2 and JA 648/15-2). The authors are grateful to Martin Winter and his team at MEET, Münster/Germany, for excellent coordination of the joint research program and to all members of the program for continuous fruitful collaboration.

Experimental

Lithium iron phosphate (LFP)

All chemicals have been purchased from Sigma Aldrich or Merck and have been used without further purification. Mesoporous SBA-15 and KIT-6 silica and CMK-3 and CMK-8 carbons were synthesized following synthesis described elsewhere [10–12]. For the composites the synthesis was as follows: 0.5 g CMK-3 were impregnated up to 12 times by the incipient wetness method, using an aqueous solution (1 M) of LiNO_3 , $(\text{NH}_4)_2\text{HPO}_4$ and $\text{FeNO}_3 \cdot 9\text{H}_2\text{O}$ for impregnation. The amount of solution used for each impregnation step was calculated to fit exactly into the pore volume of the carbon. After each impregnation step the sample was dried at 120 °C for 30 min. With completely impregnated samples of LFP composites a thermal conversion was carried out between 600 °C and 700 °C in forming gas atmosphere (N_2/H_2 95:5) for 6 h.

For carbons made with the EISA process PU foam with a density of 25 g cm^{-3} was used. A typical preparation of resol was: 3.55 g (37.7 mmol) phenol was melted and 0.65 g (3.3 mmol) of an aqueous solution of sodium hydroxide (20 wt%) was added. After 10 min of stirring 5.26 g (64.7 mmol) of formalin (37 wt% formaldehyde) was added drop wise within 5 min below 50 °C. Afterward the solution was stirred for 1 h at 70 °C. After cooling to room temperature the solution was neutralized with HCl (1 M) and the water was removed under reduced pressure. The product was dissolved to give a 20 wt% solution in ethanol. The PU foam was infiltrated with the resol solution and dried at room temperature for 12 h followed by heat treatment for 6 h at 100 °C and 160 °C respectively. Carbonizations were carried out in argon atmosphere. The temperature program was 350 °C heating for 5 h followed by 2 h at 900 °C.

For carbons PCM-PU-T-A and PCM-PU-T-B pluronic F127 were dissolved in ethanol and HCl. Followed by addition of TEOS and the resol solution (phenol/NaOH/formalin/F127/TEOS/HCl ratio was 1:0.1:2:0.013:1:0.02 for PCM-PU-T-A and 1:0.1:2:0.025:3.1:0.04 for PCM-PU-T-B). This solution was stirred for 5 h before the PU foam was infiltrated with it. Impregnation of the PU foam, carbonization and filling with LFP was carried out as described above.

Lithium nickel manganese spinel (LNMO)

Material synthesis: Bulk material was synthesized by solid state reaction. LiNO_3 , $\text{Ni}(\text{NO}_3)_2 \cdot 6\text{H}_2\text{O}$, and $\text{Mn}(\text{NO}_3)_2 \cdot 4\text{H}_2\text{O}$ were ground in a molar ratio of 1.06:0.5:1.5 to form a homogenous powder. Afterward the mixture was heated in a tube furnace in air at temperatures ranging from 700 to 900 °C. Mesoporous $\text{LiNi}_{0.5}\text{Mn}_{1.5}\text{O}_4$ (mp-LNMO) was synthesized by two different ways. One mp-LNMO was supported by KIT-6 silica as hard template. 1.0 g mesoporous silica was suspended in 50 mL of iso-hexane and stirred vigorously for 3 h 1 mL of a 1.5 M aqueous solution of LiNO_3 , $\text{Ni}(\text{NO}_3)_2 \cdot 6\text{H}_2\text{O}$

and $\text{Mn}(\text{NO}_3)_2 \cdot 4\text{H}_2\text{O}$ in molar ratios of 1.06:0.5:1.5 was added drop wise to the solution containing KIT-6 silica and stirred again overnight. The solid was filtered off, washed and dried at room temperature. Thermal conversion was carried out at temperatures from 700 to 900 °C in a tube furnace in air. Afterward the silica template was removed by treatment with 2 M sodium hydroxide solution at 70 °C overnight. The product was filtered off and washed, followed by drying at room temperature. For carbon supported material with CMK-3 or CMK-8 carbon template, the infiltration of precursor solution was carried out by the *incipient wetness* method. 0.5 g of carbon was mixed with a 1.5 M solution of LiNO_3 , $\text{Ni}(\text{NO}_3)_2 \cdot 6\text{H}_2\text{O}$ and $\text{Mn}(\text{NO}_3)_2 \cdot 4\text{H}_2\text{O}$ in molar ratios of 1.06:0.5:1.5 in ethanol or DMF to give a homogenous blend. The volume of the added solution corresponded to the actual pore volume of the used carbon. The mixture was preheated at 250 °C for 10 h and then heated at 450 °C for 10 h in air to yield mesoporous $\text{LiNi}_{0.5}\text{Mn}_{1.5}\text{O}_4$.

Thin films: LNMO thin films were prepared by pulsed laser deposition using a KrF excimer laser (*COHERENT*, $\lambda = 248$ nm). YSZ single crystals (*CrysTec, Germany*) prior covered with platinum as current collector were used as substrates. The Pt films were also deposited by PLD at 400 °C under argon atmosphere ($p(\text{Ar}) = 3 \cdot 10^{-3}$ mbar), whereas oxygen background gas ($p(\text{O}_2) = 5 \cdot 10^{-2}$ mbar) and temperatures between 950 °C and 1000 °C were used for LNMO ablation to maintain the oxygen stoichiometry of the spinel. Both platinum and LNMO films were about 50 nm thick.

Materials characterization

Powder X-ray diffraction was measured using a *PANalytical X'Pert Pro MPD* with monochromatic $\text{Cu K}\alpha$ radiation (40 kV, 45 mA). Nitrogen physisorption measurements were made with a *Quantachrome Quadrasorb SI* at a bath temperature of 77 K. Confocal XRF XANES experiments were performed at the scanning XRF microprobe installed at Beamline L at HASYLAB (Hamburg, Germany). ICP-OES analyses were carried out at a *Spectro Cirrus* inductive coupled plasma spectrometer. Thermal analysis and differential scanning calorimetry was conducted by a *Netzsch STA 449 F3 Jupiter*® heat-flux differential scanning calorimeter in pierced aluminum crucibles with a gas flow of approx. 250 mL min^{-1} . ${}^7\text{Li}$ MAS NMR experiments were carried out at an operating frequency of 155.80 MHz on a *Bruker Avance II* 400 spectrometer equipped with 4 mm double resonance probe. Spectra were acquired at room temperatures with single pulse experiments using 90° pulse length of 3.3 μs and typical delay times of 2 s. Spinning speeds were 13.5 kHz. All ${}^7\text{Li}$ NMR spectra were referenced to 1 M LiCl aqueous solution at 0 ppm.

For the SIMS measurements we used a *ToF-SIMS*® machine from *IonTOF* equipped with a bismuth primary ion source and a cesium sputter gun in the depth profiling mode. Since air contact can influence or even destroy electrode surface films, cells were disassembled in an argon-filled glovebox and transferred to the SIMS chamber in a gastight box.

Electrochemical testing

For electrochemical tests *swagelok* type T-cells were used. Cathodes contained up to 80% of active material, 10% of conducting carbon (Super P; Timcal) and 10% of PvdF binder (70:20:10 for $\text{LiNi}_{0.5}\text{Mn}_{1.5}\text{O}_4$ cathodes) and were casted on an aluminum current collector. Lithium metal was used for both the anode and the reference electrode. As electrolyte 1 M LiPF_6 in EC/DMC 1:1 w/w was used (*LP30 Merck*, Darmstadt, Germany). The assembled cells were then cycled with a *Maccor Series 4000 Automated Test System*

(Maccor Inc., Tulsa, OK, USA). Cyclic voltammograms were recorded with a Biologic VMP-3 potentiostat.

Electrochemical testing of LMNO thin films was performed in pouch-bag cells with LNMO thin films as working and lithium metal as counter electrode; as the used YSZ single crystal had a square area of 1 cm × 1 cm. As electrolyte 1 M LiPF₆ in EC/DMC 1:1 w/w was used (LP30 Merck, Darmstadt, Germany). All cells were assembled and vacuum-sealed in an argon-filled glovebox.

References

- [1] Sing KSW, Everett DH, Haul RAW, Moscou L, Pierotti RA, Rouquerol J, et al. Reporting physisorption data for gas/solid systems with special reference to the determination of surface area and porosity. *Pure Appl Chem* 1985;57:603–19.
- [2] Franger S, Le Cras F, Bourbon C, Rouault H. LiFePO₄ synthesis routes for enhanced electrochemical performance. *Electrochim Solid State Lett* 2002;5:A231–3.
- [3] Yi TF, Li CY, Zhu YR, Zhu RS, Shu J. Electrochemical intercalation kinetics of lithium ions for spinel LiNi_{0.5}Mn_{1.5}O₄ cathode material. *Russ J Electrochem* 2010;46:227–32.
- [4] Seyedhosseini zadeh H, Mahboubi F, Azadmehr A. Diffusion mechanism of lithium ions in LiNi_{0.5}Mn_{1.5}O₄. *Electrochim Acta* 2013;108:867–75.
- [5] Haetge J, Hartmann P, Brezesinski K, Janek J, Brezesinski T. Ordered large-pore mesoporous Li₄Ti₅O₁₂ spinel thin film electrodes for application in high rate rechargeable lithium batteries and hybrid supercapacitors: relationships among charge storage, electrical conductivity and nanoscale structure. *Chem Mater* 2011;23:4384–93.
- [6] Padhi A, Nanjundaswamy K, Goodenough JB. Phospho-olivines as positive-electrode materials for rechargeable lithium batteries. *J Electroch Soc* 1997;144:1188–94.
- [7] Li H, Huang XJ, Chen LQ, Zhou GW, Zhang Z, Yu DP, et al. The crystal structural evolution of nano-Si anode caused by lithium insertion and extraction at room temperature. *Solid State Ionics* 2000;135:181–91.
- [8] Erk C, Brezesinski T, Sommer H, Schneider R, Janek J. Towards silicon anodes for next-generation lithium ion batteries: a comparative performance study of various polymer binders and silicon nanopowders. *ACS Appl Mater Interfaces* 2013;5:7299–307.
- [9] Schüth F. Endo- and exotemplating to create high-surface-area inorganic materials. *Angew Chem Int Ed* 2003;42:3604–22.
- [10] Zhao D, Feng J, Huo X, Melosh N, Fredrickson GH, Chmelka FB, et al. Triblock copolymer syntheses of mesoporous silica with periodic 50 to 300 angstrom pores. *Science* 1998;279:548–52.
- [11] Kleitz F, Choi H, Ryoo R. Cubic Ia³d large mesoporous silica: synthesis and replication to platinum nanowires, carbon nanorods and carbon nanotubes. *Chem Commun* 2003;17:2136–7.
- [12] Jun S, Joo SH, Ryoo R, Kruk M, Jaroniec M, Liu Z, et al. Synthesis of new, nanoporous carbon with hexagonally ordered mesostructure. *J Am Chem Soc* 2000;122:10712–3.
- [13] Meng Y, Gu D, Zhang F, Shi Y, Cheng L, Feng D, et al. A family of highly ordered mesoporous polymer resin and carbon structures from organic–organic self-assembly. *Chem Mater* 2006;18:4447–64.
- [14] Gao F, Lu Q, Zhao D. Synthesis of crystalline mesoporous cds semiconductor nanoarrays through a mesoporous SBA-15 silica template technique. *Adv Mater* 2003;15:739–42.
- [15] Imperor-Clerc M, Bazin D, Appay MD, Beaunier P, Davidson A. Crystallization of β-MnO₂ nanowires in the pores of SBA-15 silicas: in situ investigation using synchrotron radiation. *Chem Mater* 2004;16:1813–21.
- [16] Jiao K, Zhang B, Yue B, Ren Y, Liu SX, Yan SR, et al. Growth of porous single-crystal Cr₂O₃ in a 3-D mesopore system. *Chem Commun* 2005;45:5618–20.
- [17] Crowley TA, Ziegler KJ, Lyons DM, Erts D, Olin H, Morris MA, et al. Synthesis of metal and metal oxide nanowire and nanotube arrays within a mesoporous silica template. *Chem Mater* 2003;15:3518–22.
- [18] Yue WB, Zhou WZ. Synthesis of porous single crystals of metal oxides via a solid–liquid route. *Chem Mater* 2007;19:2359–63.
- [19] Jongh PE, Eggenhuizen TM. Melt infiltration: an emerging technique for the preparation of novel functional nanostructured materials. *Adv Mater* 2013;25:6672–90.
- [20] Lim S, Yoon CS, Cho J. Synthesis of nanowire and hollow LiFePO₄ cathodes for high-performance lithium batteries. *Chem Mater* 2008;20:4560–4.
- [21] Zhu K, Yue B, Zhou W, He H. Preparation of three-dimensional chromium oxide porous single crystals templated by SBA-15. *Chem Commun* 2003;1:98–9.
- [22] Tian B, Liu X, Yang H, Xie S, Yu C, Tu B, et al. General synthesis of ordered crystallized metal oxide nanoarrays replicated by microwave-digested mesoporous silica. *Adv Mater* 2003;15:1370–4.
- [23] Valdés-Solís T, Fuertes AB. High-surface area inorganic compounds prepared by nanocasting techniques. *Mater Res Bull* 2006;41:2187–97.
- [24] Ren Y, Ma Z, Qian L, Dai S, He H, Bruce PG. Ordered crystalline mesoporous oxides as catalysts for CO oxidation. *Catal Lett* 2009;131:146–54.
- [25] Tüysüz H, Comotti M, Schüth F. Ordered mesoporous Co₃O₄ as highly active catalyst for low temperature CO-oxidation. *Chem Commun* 2008;34:4022–4.
- [26] Sun SJ, Gao QM, Wang HL, Zhu JK, Guo HL. Influence of textural parameters on the catalytic behavior for CO oxidation over ordered mesoporous Co₃O₄. *Appl Catal B* 2010;97:284–91.
- [27] Tsonecheva T, Roggenbuck J, Tiemann M, Ivanova L, Paneva D, Mitov I, et al. Iron oxide nanoparticles supported on mesoporous MgO and CeO₂: a comparative physicochemical and catalytic study. *Microporous Mesoporous Mater* 2008;110:339–46.
- [28] Zukalová M, Zukal A, Kavan L, Nazeeruddin MK, Liska P, Grätzel M. Organized mesoporous TiO₂ films exhibiting greatly enhanced performance in dye-sensitized solar cells. *Nano Lett* 2005;5:1789–92.
- [29] Jiao F, Bao J, Hill AH, Bruce PG. Synthesis of ordered mesoporous Li–Mn–O spinel as a positive electrode for rechargeable lithium batteries. *Angew Chem Int Ed* 2008;47:9711–6.
- [30] Jiao F, Shaju KM, Bruce PG. Synthesis of nanowire and mesoporous low-temperature LiCoO₂ by a post-templating reaction. *Angew Chem Int Ed* 2005;44:6550–3.
- [31] Park Y, Shin W, Lee J. Synthesis of mesoporous Li–Mn spinel without post-template treatment. *Microporous Mesoporous Mater* 2012;153:137–41.
- [32] Yang L, Ravel B, Lucht BL. Electrolyte reactions with the surface of high voltage LiNi_{0.5}Mn_{1.5}O₄ cathodes for lithium-ion batteries. *Electrochim Solid State Lett* 2010;13(8):A95–7.
- [33] Baggetto L, Unocic RR, Dudney NJ, Veit GM. Fabrication and characterization of Li–Mn–Ni–O sputtered thin film high voltage cathodes for Li-ion batteries. *J Power Sources* 2012;211:108–18.
- [34] Maxisch T, Zhou F, Ceder G. Ab initio study of the migration of small polarons in olivine Li₄FePO₄ and their association with lithium ions and vacancies. *Phys Rev B* 2006;73:104301–1–104301–6.
- [35] Goodenough JB, Kim Y. Challenges for rechargeable Li batteries. *Chem Mater* 2010;22:587–603.
- [36] Ravet N, Chouinard Y, Magnan JF, Besner S, Gauthier M, Armand M. Electroactivity of natural and synthetic triphylite. *J Power Sources* 2001;97–98:503–7.
- [37] Wang Y, Wang Y, Hosono E, Wang K, Zhou H. The design of a LiFePO₄/carbon nanocomposite with a core–shell structure and its synthesis by an in situ polymerization restriction method. *Angew Chem Int Ed* 2008;47:7461–5.
- [38] Yang J, Wang J, Tang Y, Wang D, Xiao B, Li X, et al. In situ self-catalyzed formation of core–shell LiFePO₄@CNT nanowires for high rate performance lithium-ion batteries. *J Mater Chem A* 2013;1:7306–11.
- [39] Doeff MM, Hu Y, McLarnon F, Kostecki R. Effect of surface carbon structure on the electrochemical performance of LiFePO₄. *Electrochim Solid State Lett* 2003;6:A207–9.
- [40] Dominko R, Bele M, Gaberscek M, Remskar M, Hanzel D, Pejovnik S, et al. Impact of the carbon coating thickness on the electrochemical performance of LiFePO₄/C composites. *J Electroch Soc* 2005;152:A607–10.
- [41] Pan F, Chen X, Li H, Xin X, Chang Q, Jiang K, et al. Influence of carbon coating porosity on the electrochemical performance of LiFePO₄ cathode. *Electrochim Commun* 2011;13:726–9.
- [42] Yuan LX, Wang ZH, Zhang WX, Hu XL, Chen JT, Huang YH, et al. Development and challenges of LiFePO₄ cathode material for lithium-ion batteries. *Energy Environ Sci* 2011;4:269–84.
- [43] Wang J, Sun X. Understanding and recent development of carbon coating on LiFePO₄ cathode materials for lithium-ion batteries. *Energy Environ Sci* 2012;5:5163–85.
- [44] Hasegawa G, Ishihara Y, Kanamori K, Miyazaki K, Yamada Y, Nakanishi K, et al. Facile preparation of monolithic LiFePO₄/carbon composites with well-defined macropores for a lithium-ion battery. *Chem Mater* 2011;23:5208–16.
- [45] Liang C, Li Z, Dai S. Mesoporous carbon materials: synthesis and modification. *Angew Chem Int Ed* 2008;47:3696–717.
- [46] Thomas A, Goettmann F, Antonietti M. Hard templates for soft materials: creating nanostructured organic materials. *Chem Mater* 2008;20(3):738–55.
- [47] Upare DP, Yoon S, Lee CW. Nano-structured porous carbon materials for catalysis and energy storage. *Korean J Chem Eng* 2011;28(3):731–43.
- [48] Shen W, Fan W. Nitrogen-containing porous carbons: synthesis and application. *J Mater Chem A* 2013, 1, 999–1013.
- [49] Canderlaria SL, Shao Y, Thou W, Li Y, Xiao J, Thang JG, et al. Nanostructured carbon for energy storage and conversion. *Nano Energy* 2012;1:195–220.
- [50] Jiang H, Lee PS, Li C. 3D carbon based nanostructures for advanced supercapacitors. *Energy Environ Sci* 2013;6:41–53.
- [51] Doherty CM, Caruso RA, Smarsly BM, Adelhelm P, Drummond CJ. Hierarchically porous monolithic LiFePO₄/carbon composite electrode materials for high power lithium ion batteries. *Chem Mater* 2009;21:5300–6.
- [52] Dimesso L, Spanheimer C, Jacke S, Jaegermann W. Synthesis and characterization of three-dimensional carbon foams–LiFePO₄ composites. *J Power Sources* 2011;196:6729–34.
- [53] Dimesso L, Jacke S, Spanheimer C, Jaegermann W. Investigation on 3-dimensional carbon foams/LiFePO₄ composites as function of the annealing time under inert atmosphere. *J Alloys Compd* 2011;509:3777–82.
- [54] Mizushima K, Jones PC, Wiseman PJ, Goodenough JB. Li_xCoO₂ (0 < x < 1): a new cathode material for batteries of high energy density. *Mater Res Bull* 1980;15:783–9.
- [55] Patoux S, Daniel L, Bourbon C, Lignier H, Pagano C, Le Cras F, et al. High voltage spinel oxides for Li-ion batteries: from the material research to the application. *J Power Sources* 2009;189:344–52.
- [56] Pasero D, Reeves N, Pralong V, West AR. Oxygen nonstoichiometry and phase transitions in LiMn_{1.5}Ni_{0.5}O_{4–δ}. *J Electrochim Soc* 2008;155:A282–91.

[57] Kim J, Myung S, Yoon CS, Kang SG, Sun Y. Comparative study of $\text{LiNi}_{0.5}\text{Mn}_{1.5}\text{O}_{4-\delta}$ and $\text{LiNi}_{0.5}\text{Mn}_{1.5}\text{O}_4$ cathodes having two crystallographic structures: $Fd\bar{3}m$ and $P4_332$. *Chem Mater* 2004;16:906–14.

[58] Wang L, Li H, Huang X, Baudrin E. A comparative study of $Fd\bar{3}m$ and $P4_332$ “ $\text{LiNi}_{0.5}\text{Mn}_{1.5}\text{O}_4$ ”. *Solid State Ionics* 2011;193:32–8.

[59] McCalla E, Dahn JR. The spinel and cubic rocksalt solid-solutions in the Li–Mn–Ni oxide pseudo-ternary system. *Solid State Ionics* 2013;242:1–9.

[60] McCalla E, Rowe AW, Shunmugasundaram R, Dahn JR. Structural study of the Li–Mn–Ni oxide pseudoternary system of interest for positive electrodes of Li-ion batteries. *Chem Mater* 2013;25:989–99.

[61] Kim JH, Myung ST, Yoon CS, Oh IH, Sun YK. Effect of Ti substitution for Mn on the structure of $\text{LiNi}_{0.5}\text{Mn}_{1.5-x}\text{Ti}_x\text{O}_4$ and their electrochemical properties as lithium insertion material. *J Electrochem Soc* 2004;151:A1911–8.

[62] Arunkumar TA, Manthiram A. Influence of chromium doping on the electrochemical performance of the 5 V spinel cathode $\text{LiMn}_{1.5}\text{Ni}_{0.5}\text{O}_4$. *Electrochim Acta* 2005;50:5568–72.

[63] Zheng M, Cao J, Liao S, Liu J, Chen H, Zhao Y, et al. Preparation of mesoporous Co_3O_4 nanoparticles via solid–liquid route and effects of calcination temperature and textural parameters on their electrochemical capacitive behaviors. *J Phys Chem C* 2009;113:3887–94.

[64] Alcántara R, Jaraba M, Lavela P, Lloris JM, Pérez Vicente C, Tirado JL. Synergistic effects of double substitution in $\text{LiNi}_{0.5-y}\text{Fe}_y\text{Mn}_{1.5}\text{O}_4$ spinel as 5 V cathode materials. *J Electrochem Soc* 2005;152:A13–8.

[65] Leon B, Lloris JM, Vicente CP, Tirado JL. Structure and lithium extraction mechanism in $\text{LiNi}_{0.5}\text{Mn}_{1.5}\text{O}_4$ after double substitution with iron and titanium. *Electrochim Solid State Lett* 2006;9(2):A96–100.

[66] Alcántara R, Jaraba M, Lavela P, Tirado JL. Structural and electrochemical study of new $\text{LiNi}_{0.5}\text{Ti}_x\text{Mn}_{1.5-x}\text{O}_4$ spinel oxides for 5-V cathode materials. *Chem Mater* 2003;15:2376–82.

[67] Sun YK, Hong KJ, Prakash J, Amine K. Electrochemical performance of nanosized ZnO-coated $\text{LiNi}_{0.5}\text{Mn}_{1.5}\text{O}_4$ spinel as 5 V materials at elevated temperatures. *Electrochim Commun* 2002;4:344–8.

[68] Arrebara JC, Caballero A, Hernan L, Melero M, Morales J, Castellon ER. Electrochemical properties of $\text{LiNi}_{0.5}\text{Mn}_{1.5}\text{O}_4$ films prepared by spin-coating deposition. *J Power Sources* 2006;162(1):606–13.

[69] Xia H, Lu L. Li diffusion in spinel $\text{LiNi}_{0.5}\text{Mn}_{1.5}\text{O}_4$ thin films prepared by pulsed laser deposition. *Phys Scr* 2007;T129:43–8.

[70] Xia H, Tang SB, Lu L, Meng YS, Ceder G. The influence of preparation conditions on electrochemical properties of $\text{LiNi}_{0.5}\text{Mn}_{1.5}\text{O}_4$ thin film electrodes by PLD. *Electrochim Acta* 2007;52:2822–8.

[71] Mohamedi M, Makino A, Dokko K, Itoh T, Uchida I. Electrochemical investigation of $\text{LiNi}_{0.5}\text{Mn}_{1.5}\text{O}_4$ thin film intercalation electrodes. *Electrochim Acta* 2002;48:79–84.

[72] Wang J, Xue C, Lv Y, Zhang F, Tu B, Zhao D. Kilogram-scale synthesis of ordered mesoporous carbons and their electrochemical performance. *Carbon* 2011;49:4580–8.

[73] Liu R, Shi Y, Wan Y, Meng Y, Zhang F, Gu D, et al. Triconstituent co-assembly to ordered mesostructured polymer–silica and carbon–silica nanocomposites and large-pore mesoporous carbons with high surface areas. *J Am Chem Soc* 2006;128:11652–62.

[74] Ren Y, Armstrong AR, Jiao F, Bruce PG. Influence of size on the rate of mesoporous electrodes for lithium batteries. *J Am Chem Soc* 2010;132:996–1004.

[75] Aurbach D, Markovsky B, Salitra G, Markevich E, Talyossef Y, Koltypin M, et al. Review on electrode–electrolyte solution interactions, related to cathode materials for Li-ion batteries. *J Power Sources* 2007;165:491–9.

[76] Menzel M, Schifke A, Falk M, Janek J, Fröba M, Fittschen UEA. Surface and in-depth characterization of lithium-ion batteries cathodes at different cycle states using confocal micro-X-ray fluorescence–X-ray absorption near edge structure analysis. *Spectrochim Acta B* 2013;85:62–70.

[77] Aurbach D, Markovsky B, Talyossef Y, Salitra G, Hyeong-Jin K, Seungdon C. Studies of cycling behavior, ageing, and interfacial reactions of $\text{LiNi}_{0.5}\text{Mn}_{1.5}\text{O}_4$ and carbon electrodes for lithium-ion 5-V cells. *J Power Sources* 2006;162:780–9.

[78] Lee YJ, Eng C, Grey CP. ^{6}Li magic angle spinning NMR study of the cathode material $\text{LiNi}_x\text{Mn}_{2-x}\text{O}_4$: the effect of ni doping on the local structure during charging. *J Electrochem Soc* 2001;148:A249–57.

[79] Wu X, Li X, Wang Z, Guo H, Yue P. Capacity fading reason of $\text{LiNi}_{0.5}\text{Mn}_{1.5}\text{O}_4$ with commercial electrolyte. *Ionics* 2013;19:379–83.

[80] Edström K, Gustafsson T, Thomas JO. The cathode–electrolyte interface in the Li-ion battery. *Electrochim Acta* 2004;50(2–3):397–403.

[81] Xu K. Electrolytes and interphasial chemistry in li ion devices. *Energy* 2010;3:135–54.

[82] Eriksson T, Andersson AM, Gejke C, Gustafsson T, Thomas JO. Influence of temperature on the interface chemistry of $\text{Li}_x\text{Mn}_2\text{O}_4$ electrodes. *Langmuir* 2002;18(9):3609–19.

[83] Winter M, Besenhard JO, Spahr ME, Novak P. Insertion electrode materials for rechargeable lithium batteries. *Adv Mater* 1998;10(10):725–63.